RESEARCH

High-fidelity-generalized-method-of-cells micromechanical analysis of damage evolution in viscoelastic composites

Nathan Perchikov[1] · Jacob Aboudi[1] · Konstantin Y. Volokh[2]

Abstract

The effect of time-delayed stress response, typical for viscoelastic materials, on the evolution of damage in porous soft materials and fiber-reinforced soft-matrix composites is studied by employing the material-sink gradual damage evolution theory and the micromechanical finite strain high-fidelity generalized method of cells (HFGMC). In the material-sink approach, damage and crack locations are not postulated in advance, but are instead predicted by the solution of a two-way coupled system of mechanistically derived differential equations, which include the intact-material balance law, in addition to stress equilibrium. The viscoelastic response is based on a rheological model of the generalized Maxwell type, typical for biological tissues. The viscoelastic constitutive relation is generalized to incorporate evolving damage, resulting in loading-rate sensitive time-dependent response. The finite strain HFGMC micromechanics analyzes composite materials that possess periodic microstructure and are comprised of constituents characterized by complex response, with a viscous part, a hyperelastic part and a degradation part, described by a phase-field like approach, albeit derived mechanistically. In the framework of HFGMC micromechanics, the repeating unit cell of the periodic composite is divided into numerous subcells. The resulting coupled system of equations is enforced in the subcell in strong form in the volume-averaged sense and the internal (continuity) and global (periodic) boundary conditions are imposed in the surface-averaged sense. Subcell equilibrium is algorithmically attained prior to fields continuity. Applications are presented for the prediction of the stress response and damage evolution history in porous soft viscoelastic materials and fiber-reinforced viscoelastic composites.

1 Introduction

Fracture and failure in materials are usually modeled by introducing sharp cracks (discontinuities) (Ritchie and Liu 2021; Dormieux and Kondo 2016) or by adding (local) damage

✉ N. Perchikov
  perchico@gmail.com

1   School of Mechanical Engineering, Faculty of Engineering, Tel Aviv University, Ramat Aviv
     69978, Israel

2   Faculty of Civil Engineering, Technion – Israel Institute of Technology, Haifa 32000, Israel

variables to the governing constitutive equations (Kachanov 1986; Murakami 2012). In the phase-field approach, on the other hand, the fracture and failure patterns are obtained by solving a coupled system of differential equations, which include an auxiliary scalar variable (the phase field) obeying a nonlocal evolution equation. In this approach, the fracture path is not known in advance, but is rather obtained from the solution of these equations. For a review of phase-field approaches see Bui and Hu (2021) and the more recent articles by Quinteros et al. (2022), Rao et al. (2022), Sangaletti and Garcia (2022), Meshi et al. (2023) and the references therein. For a review of various recent approaches to the modeling of failure and fracture in soft materials, see Volokh (2020).

Several recent studies dedicated specifically to the analysis of damage in viscoelastic materials/composites using various phase-field approaches should be noted.

We should first mention that there have been several different approaches to the problem of phase-field modeling of fracture, as far as the conceptual algorithmic/mathematical strategy is concerned. For instance, whether infinitesimal or finite elasticity should be considered; whether differential or integral form of the conservation laws should be employed; whether a multiple times-scales approach should be used, in a predictor-corrector-like fashion; whether the phase field should be defined globally or limited to a boundary-layer, etc. The following works give a sense of the conceptual-algorithmic diversity of the mathematical approaches to the problem. In Arash et al. (2021) a finite-deformation phase-field fracture model is used for the thermo-viscoelastic analysis of polymer nanocomposites. A standard phase-field approach is followed, with an incremental Jaumann objective-stress formalism. In Dammaß et al. (2023) a phase-field formalism is employed to study finite strain rate-dependent fracture in solids. A generalized Maxwell solid is assumed, with a quadratic phase field for energy degradation, Ogden's energy functionals and the staggered integration scheme of Miehe et al. (2010), with consecutive advancement of displacement and damage. In Hu et al. (2023), a nearly incompressible material with the generalized Maxwell model constitutive response is studied employing a fourth-order phase field, accounting for the Hessian of the phase field, and using a relaxed incompressibility constraint at the damaged zones. Incremental finite-element discretization is performed, also with the staggered integration scheme. In Gopalsamy et al. (2023), the authors employ a variational approach to model fracture in viscoelastic materials. In this approach, a phase-field solution is checked against a lip-field solution, which employs a Liphschitz-continuous nonsmooth field that is nonzero everywhere except in a narrow region to regularize crack microbranching. The generalized Kelvin–Voigt viscoelastic model is assumed. The staggered scheme is applied, with a triangular-mesh finite-element discretization. In Partmann et al. (2023), the peridynamics approach to kinematics is employed (i.e., one with a nonlocal integral equilibrium equation), along with a standard phase-field approximation for the representation of damage. The equilibrium equations are integrated with an energy-conserving Verlet scheme, reproducing experimentally observed cracks.

To cover the variety of relevant earlier works from the more physical perspective, several additional studies should be mentioned. In Hai et al. (2024), a phase field strategy with a rational phase field function is employed for brittle materials with account of viscoelasticity and microviscosity in a finite-element two-way coupled scheme with weights. Crack branching is observed. The approach is noteworthy due to the rate term appearing explicitly in the damage balance equation, which makes the approach more mesoscopic than the one employed in Perchikov et al. (2023) where the rate term was assumed to average to a constant on a macroscale. The branching could accordingly be interpreted as a smaller-scale phenomenon, more relevant for harder materials than the biological tissues primarily intended in Perchikov et al. (2023) and similar studies. The study in Jafarzadeh et al. (2024) investigates

crack propagation in polycrystalline materials accounting for interfacial energy between the grains, essentially solving a Ginzburg–Landau equation with multiple phase fields. A periodic setting is assumed with a dedicated Fourier solver. In Fantoni et al. (2020), a phase field approach to study damage propagation in periodic microstructured materials is implemented in a multiscale finite-element setting with asymptotic homogenization (preventing the need for heavy FE^2 calculations). Characteristic homogenized response is obtained for matrix/fibers individual degradation, with asymptotic stress decay after a peak value.

The present work differs from the cited studies in that it targets specifically periodic composites, where the governing equations are solved in the HFGMC (rather the Finite-element) approach, where local equilibrium is enforced prior to global continuity of fields, which is suitable for inequilibrium settings. Damage is modeled by use of a phase-field like variable, albeit one governed by a mechanistically-derived evolution equation entailing homogenizaton to the macro-scale, as can be assumed appropriate for composites representing biological tissue. The emerging damage is associated with loss of intact material, in line with the assumptions of the material-sink model. The material-sink model was introduced in Volokh (2017) and further motivated in Perchikov et al. (2023). It is based on the empirical observation that crack surfaces, rather than being created by the separation of two adjacent atomic layers, are more commonly the result of the breakage of several material bonds, spread over a region with a characteristic length *l*. In this approach fracture is thus assumed to lead to finite bonds-loss, or to a decrease in the mass density of intact material. Accordingly, a mass balance equation for the intact material is included in the set of governing coupled differential equations for the (coarse-grained) continuum.

The material-sink model was applied in Abu-Qbeitah et al. (2023a) to investigate quasistatic crack propagation in soft materials. This investigation was further extended for the modeling of cracks in viscoelastic materials, Abu-Qbeitah et al. (2023b). Dynamic crack propagation effects in soft materials were studied in Abu-Qbeitah et al. (2022). In Perchikov et al. (2023), the material-sink approach was implemented to study the evolution of damage in porous hyperelastic materials and fiber-reinforced composites comprised of hyperelastic constituents. In the present investigation, the analysis in Perchikov et al. (2023) is generalized to account for viscoelasticity of the solid phases in the otherwise hyperelastic composite as it experiences gradual damage. To obtain the constitutive response of viscoelastic material undergoing gradual damage, the approach in Simo (1987) is implemented with proper introduction of the damaged phase field into the equations. In order to perform consistent derivation of the appropriate constitutive response, a simplified rheological model is analyzed and used as motivation for a continuum-mechanical tensorial model, in a manner reminiscent of the one employed in Simo (1987).

As in Perchikov et al. (2023), a periodic arrangement of phases in a 2D composite is assumed. The periodicity enables the identification of a repeating unit cell (RUC), which is then analyzed. This repeating unit cell is discretized into several subcells, each of which is filled by viscoelastic material. The increment of the displacement vector in each subcell is represented as a second-order expansion (which includes the applied far-field global strain increment), in terms of local coordinates. The unknown quantities (microvariables' increments) in the expansion are determined by the enforcement of the volume averages of the equilibrium and intact-material mass conservation equations and the viscoelastic constitutive relations, and by the enforcement, in a spatial-averaged sense, of the continuity of the increments of the displacements and tractions between the subcells, as well as the global (periodic) boundary conditions (the conditions ensure that the displacements and tractions increments on opposite boundaries of the repeating unit cell are identical). Extensive discussions, validations and implementations of the finite strain HFGMC are given in chapter nine
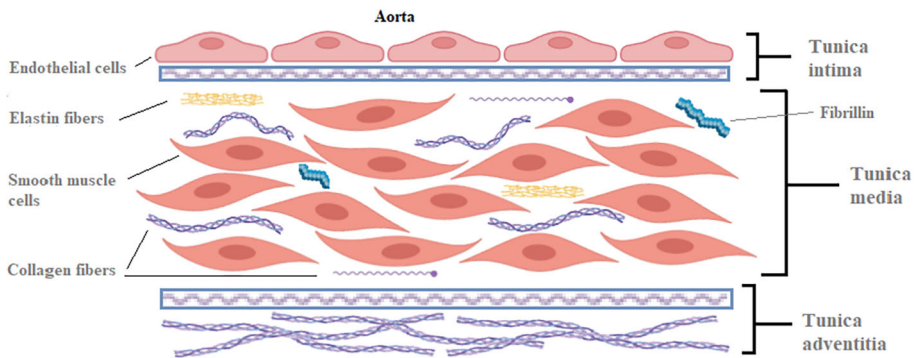
Fig. 1 A typical schematic description of the cross section of aortic fabric (with partial aneurysm), drawn in the spirit of a typical image as given in Britannica (2023), plotted with BioRender

of Aboudi et al. (2013). The HFGMC was employed in Breiman et al. (2020) for the micromechanical prediction of the behavior of soft elastic tissues and in Breiman et al. (2022) for the prediction of composites failure. The generalization of the finite strain HFGMC to include viscoelastic effects was given in Aboudi and Volokh (2020).

The offered micromechanical viscoelastic analysis is applied to investigate the damage evolution in porous materials and fiber-reinforced composites. The effects of the amount of porosity and the fibers' volume ratio are investigated, and the responses to the loading are obtained. Comparisons between the behaviors of composites in which the fibers are distributed to form square versus hexagonal arrays are presented. Finally, comparisons between regular and random distributions of the fibers in the composite are exhibited. In the corresponding figures, the effect of viscoelasticity is shown through comparison with perfectly elastic response in a similar setting.

The paper is organized as follows. Section 2 presents the rheological model serving as motivation for the employed constitutive equations. Section 3 shows the continuum theory, encompassed in the governing constitutive, equilibrium and mass conservation equations, incorporating the material-sink model. The section ends with the constitutive equations for the viscoelastic material given in incremental form. The numerical algorithm for the solution of the discretized system of PDEs, based on a predictor-corrector strategy, is given in Sect. 4. Examples solved with the proposed theory are given in Sect. 5. Section 6 concludes.

2 Motivating scalar rheological model

In the following we derive a scalar motivational model for the tensorial constitutive degrading viscoelastic continuum model that we employ in the example calculations we perform for materials common in bio-mechanical contexts.

A characteristic schematic description of the cross section of aortic fabric (with partial aneurysm) from the mechanical perspective can be seen in Fig. 1, drawn in the spirit of a typical image as given in Britannica (2023), plotted with BioRender.

In the schematic view one can identify the top and bottom envelope layers, that act as a (hyper-)elastic spring, in parallel to which the internal region of the cross section supplies additional stress in response to strain and strain rate. The internal region contains liquid, filled with short plates or fibers and short elastic springs. In response to finite strain rate, the

Fig. 2 Schematic representation of the rheological substructure
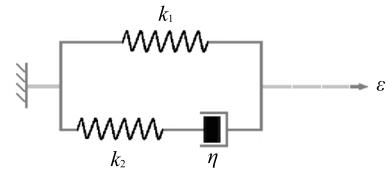
nonuniformity creates a Couette-like flow of the liquid, which generates Newtonian stress, proportional to a part of the applied strain rate, the viscous part. On the other hand, some of the applied strain rate generates strain stretching the short elastic fibers, which creates proportional stress, more or less equilibrated with the viscous stress. Some strain (rate) translates to shear viscous flow between the solid fibers, while additional strain stretches those fibers – hence the strain additivity assumption. This picture can be described in a simplified manner in the following rheological model, in which the Tunica Intima and Tunica Advetilia act as the primary spring, and in parallel to it the Tunica Media acts as a queued assembly of a dashpot and a spring, representing the internal liquid in the aorta and the short Elastin fibers.

The assumed rheological model (generalized Maxwell of rank-1) is shown below in Fig. 2.

It is assumed that the aforementioned reality holds for the intact material, but kinematically, ε represents the strain applied on a general chunk of matter, possibly including damaged spots. Therefore, the stress responses inside the substructure would be

$$S_1 = \theta k_1 \varepsilon$$

for the main spring and

$$S_2 = \theta k_2 (\varepsilon - \varepsilon_v)$$

for the secondary spring, where ε_v is the viscoelastic strain and θ is the volume fraction of intact material in a chunk of matter possibly undergoing damage (crumbling), the amount of which is related to θ (see Perchikov et al. (2023)). In turn, for the dashpot the constitutive relation would be

$$S_2 = \theta \eta \dot{\varepsilon}_v.$$

The multiplication of the three stresses by θ represents the fact that ruptured material does not have any response at all, as when the network of proteins breaks, the filling liquid undergoes decohision and loses contact with the bulk. Therefore, there is no point in retaining the viscous response represented by the dashpot when a full chunk of viscoelastic matter ruptures – hence the multiplication by θ also in the last relation. Assuming linear elastic response and time-evolving average intact-material cross section, θ, and taking a time derivative of the second relation divided by θ (and then multiplying by θ, namely, $\dot{S}_2 - S_2\dot{\theta}/\theta = \theta k_2(\dot{\varepsilon} - \dot{\varepsilon}_v)$) and substituting the dashpot relation on the right-hand side, we get the following differential equation for S_2:

$$\dot{S}_2 + \left(\frac{k_2}{\eta} - \frac{\dot{\theta}}{\theta} \right) S_2 = \theta k_2 \dot{\varepsilon} \tag{2.1}$$

This is a first-order linear differential equation of the form

$$\dot{y} + f(t) y = g(t),$$

with $f(t) \triangleq \frac{k_2}{\eta} - \frac{\dot\theta}{\theta}$ and $g(t) \triangleq \theta k_2 \dot\varepsilon$, which has the following solution for $y(0) = 0$ (Polyanin and Zaitsev 2003)

$$y(t) = e^{F(t)} \int_0^t e^{-F(\tau)} g(\tau) d\tau,$$

where

$$F(t) = - \int_0^t f(\tau) d\tau$$

In our case,

$$F(t) = \ln \frac{\theta(t)}{\theta(0)} - \frac{k_2}{\eta} t$$

and thus for $\theta(0) = 1$ we have $e^{F(t)} = \theta e^{-\frac{k_2}{\eta} t}$, and $e^{-F(\tau)} = \frac{1}{\theta} e^{\frac{k_2}{\eta} \tau}$ and thus

$$S_2(t) = \theta \int_0^t e^{-\frac{k_2}{\eta}(t-\tau)} k_2 \dot\varepsilon d\tau \qquad (2.2)$$

If we then define $\tau_2 \triangleq \frac{\eta}{k_2}$, $W^{(1)} = \frac{1}{2} k_1 \varepsilon^2$ and $W^{(2)} = \frac{1}{2} k_2 \varepsilon^2$, we get the total stress as:

$$S = \theta \frac{\partial W^{(1)}}{\partial \varepsilon} + \theta \int_0^t e^{-(t-\tau)/\tau_2} \frac{d}{d\tau} \frac{\partial W^{(2)}(\tau)}{\partial \varepsilon} d\tau \qquad (2.3)$$

In the rheological model derived herein, the additive decomposition of strain rates was assumed, which is known to hold for small strains and strain rates. For small strains and strain rates, there is also equivalence between the small strain and the Lagrangian quadratic objective strain, for example. Therefore, if the loading strain and strain rate remain small, then one can substitute in the discussed derivation the small strain by the Lagrangian strain and expect the theory to still hold.

Another remark should be made at this point. As discussed in Perchikov et al. (2023), the first Piola-Kirchhoff stress in the damaging material is acknowledged to be proportional to the relative intact material density θ. Since the deformation gradient is defined on a macroscopic infinitesimal chunk of material incorporating damaged zones, it is assumed that the deformation gradient, $\mathbf{F}$, is the extensive property shared both by intact and total amount of material, and only the stress is different. Therefore, the second Piola–Kirchhoff stress, $\mathbf{S}$, related to the first, $\mathbf{P}$, through multiplication by $\mathbf{F}$ (independent of θ) from the left, becomes also proportional to θ. Then, making the tensorial generalization of Eq. (2.3), and substituting $\mathbf{S}$ for S and $\mathbf{E}$ for ε (bearing in mind the small deformation regime), we observe that indeed $\mathbf{S}$ stays proportional to θ, as it should be.

3 Governing equations for the monolithic viscoelastic continuum

In the framework of the material damage theory as discussed in Perchikov et al. (2023), drawing motivation form the scalar model detailed in Sect. 2 and from the study in Simo

(1987), the second Piola–Kirchhoff (objective) stress tensor for a monolithic viscoelastic continuum representative of aortic fabric undergoing damage, $\mathbf{S}$, would be given by

$$\mathbf{S} = \theta \frac{\partial W^{(1)}(\mathbf{E})}{\partial \mathbf{E}} + \theta \int_0^t \exp\left(-\frac{t-\tau}{\tau_2}\right) \frac{d}{d\tau} \frac{\partial W^{(2)}(\mathbf{E})}{\partial \mathbf{E}} \, d\tau, \tag{3.1}$$

where $W^{(1)}$ is the elastic strain energy at equilibrium and $\mathbf{E} = \frac{1}{2}\left(\mathbf{F}^T\mathbf{F} - \mathbf{I}\right)$ is the Lagrangian objective strain tensor.

For simplicity, it is assumed that the term $W^{(2)}(\mathbf{E})$ is proportional to $W^{(1)}(\mathbf{E})$ with a scalar constant multiplier, namely $W^{(2)}(\mathbf{E}) = \bar{\delta} W^{(1)}(\mathbf{E})$ (this assumption means that we assume that the different elastic parts of the fabric have similar strain dependence, presumably due to similar internal structure, but possibly with different density, which is reflected by proportional scaling of the tangent moduli).

Thus,

$$\mathbf{S}(t) = \theta \frac{\partial W^{(1)}(\mathbf{E})}{\partial \mathbf{E}} + \bar{\delta}\theta \int_0^t \exp\left(-\frac{t-\tau}{\tau_2}\right) \frac{d}{d\tau} \frac{\partial W^{(1)}(\mathbf{E})}{\partial \mathbf{E}} \, d\tau \tag{3.2}$$

For algorithmic efficiency, the convolution integral should be approximated numerically. To this end, it would be beneficial to first present it as a pure integral over given functions.

We are primarily interested here in modeling fracture in viscoelastic materials, where damage generates and evolves on a shorter time scale than the time scale of viscous relaxation. If damage evolves slower than viscous internal motion, then it is either negligible viscosity, as addressed in Perchikov et al. (2023), or very gradual damage not evolving into crack-like patterns, in which case it is outside the scope of the present work. Under these assumptions, as shown in Appendix A, it is possible to present the 2nd Piola–Kirchhoff stress in the following form:

$$\begin{aligned}
\mathbf{S}(t) &= \mathbf{S}^{(1)}(t) + \mathbf{\Psi}^{(2)}(t), \\
\mathbf{S}^{(1)}(t) &\triangleq \theta(t) \frac{\partial W^{(1)}(\mathbf{E}(t))}{\partial \mathbf{E}}, \\
\mathbf{\Psi}^{(2)}(t) &\triangleq \bar{\delta} \int_0^t \exp\left(-\frac{t-\tau}{\tau_2}\right) \dot{\mathbf{S}}^{(1)}(\tau) \, d\tau.
\end{aligned} \tag{3.3}$$

It can then be shown (Simo and Hughes 1998) that the following approximation can be established for $\mathbf{\Psi}^{(2)}$ at time t:

$$\begin{aligned}
\mathbf{\Psi}^{(2)}(t) = {}& \bar{\delta} \frac{\mathbf{S}^{(1)}(t) - \mathbf{S}^{(1)}(t-\Delta t)}{\Delta t} \tau_2 \left[1 - \exp\left(-\frac{\Delta t}{\tau_2}\right)\right] \\
&+ \exp\left(-\frac{\Delta t}{\tau_2}\right) \mathbf{\Psi}^{(2)}(t-\Delta t),
\end{aligned} \tag{3.4}$$

where Δt is a sufficiently small time increment. Hence, the following expression for the increment of $\mathbf{\Psi}^{(2)}(t)$ can be obtained:

$$\Delta\mathbf{\Psi}^{(2)}(t) = \beta_2 \bar{\delta} \Delta\mathbf{S}^{(1)}(t) - \alpha_2 \mathbf{\Psi}^{(2)}(t-\Delta t), \quad \Delta\mathbf{S}^{(1)}(t) \triangleq \mathbf{S}^{(1)}(t) - \mathbf{S}^{(1)}(t-\Delta t), \tag{3.5}$$

where $\alpha_2 = 1 - \exp(-\frac{\Delta t}{\tau_2})$, $\beta_2 = \alpha_2 \tau_2 / \Delta t$. This recursive relation is employed to update the variables at every increment.

In addition to the 2nd Piola–Kirchhoff stress, the theory requires the mass flux of damaged material, **s**, which is given by Perchikov et al. (2023):

$$\mathbf{s} = l^2 \nabla \theta, \tag{3.6}$$

where l is an appropriate coefficient, representative of the thickness of a developed crack.

Due to the nonlinearity of the objective tensorial formulation in view of possible large rotations of some material points (due to damage), the constitutive equations must be formulated and applied in incremental form. To this end, first, the representative isotropic hyperelastic function $W^{(1)}$ is usually expressed in terms of the three invariants I_1, I_2, and I_3 of the left Cauchy–Green deformation tensor $\mathbf{C} = \mathbf{F}^\top \mathbf{F}$, which are given as follows:

$$I_1 = \text{tr}\,(\mathbf{C}), \quad I_2 = \frac{1}{2}\left(\text{tr}^2\mathbf{C} - \text{tr}\,\mathbf{C}^2\right), \quad I_3 = \det\,(\mathbf{C}) \tag{3.7}$$

Hence

$$\Delta\frac{\partial W^{(1)}}{\partial \mathbf{E}} = \frac{1}{2}\mathbb{D}^{(1)} : \Delta\mathbf{C}, \tag{3.8}$$

where the fourth-order tangent tensor is given by

$$\mathbb{D}^{(1)} = 4\frac{\partial^2 W^{(1)}}{\partial\mathbf{C}\partial\mathbf{C}}. \tag{3.9}$$

It should be noted that since $W^{(1)} = W^{(1)}(I_1, I_2, I_3)$, it follows that

$$\frac{\partial W^{(1)}}{\partial\mathbf{C}} = \sum_{p=1}^{3}\frac{\partial W^{(1)}}{\partial I_p}\frac{\partial I_p}{\partial\mathbf{C}}, \tag{3.10}$$

where the expressions for $\partial I_p/\partial\mathbf{C}$ and $\partial^2 I_p/(\partial\mathbf{C}\partial\mathbf{C})$, required for the evaluation of $\partial^2 W^{(1)}/(\partial\mathbf{C}\partial\mathbf{C})$ can be found in Aboudi et al. (2013).

It follows from Eq. (3.3) that the increment of $\mathbf{S}^{(1)}$ takes the form

$$\Delta\mathbf{S}^{(1)} = \frac{\theta}{2}\mathbb{D}^{(1)} : \Delta\mathbf{C} + 2\Delta\theta\frac{\partial W^{(1)}}{\partial\mathbf{C}} \tag{3.11}$$

Equation (3.3) also yields the following expression for the increment of $\mathbf{S}$:

$$\Delta\mathbf{S}(t) = \Delta\mathbf{S}^{(1)} + \Delta\boldsymbol{\Psi}^{(2)}(t), \tag{3.12}$$

which in conjunction with Eq. (3.5) yields:

$$\Delta\mathbf{S} = (1 + \gamma)\,\Delta\mathbf{S}^{(1)} - \Delta\mathbf{Q}, \tag{3.13}$$

where $\gamma = \beta_2\bar{\delta}$, and

$$\Delta\mathbf{Q} = \alpha_2\boldsymbol{\Psi}^{(2)}(t - \Delta t). \tag{3.14}$$

The first Piola–Kirchhoff stress tensor $\mathbf{T}$ is then given by Malvern (1969)

$$\mathbf{T} = \mathbf{S}\mathbf{F}^\top. \tag{3.15}$$

By utilizing Eqs. (3.13) and (3.11), the following expression for $\Delta\mathbf{T}$ can be established:

$$\Delta\mathbf{T} = \frac{(1+\gamma)}{2}\theta\left(\mathbb{D}^{(1)} : \Delta\mathbf{C}\right)\mathbf{F}^\top + \mathbf{S}\Delta\mathbf{F}^\top$$

$$+ 2\left(1+\gamma\right)\Delta\theta\frac{\partial W^{(1)}}{\partial\mathbf{C}}\mathbf{F}^\top - (\Delta\mathbf{Q})\mathbf{F}^\top. \tag{3.16}$$

After some manipulations, the increment of the first Piola–Kirchhoff stress tensor can be written as:

$$\Delta\mathbf{T} = \mathbb{R} : \Delta\mathbf{F} + \mathbf{H}\Delta\theta - \Delta\mathbf{V}. \tag{3.17}$$

In this equation, the fourth-order tensor $\mathbf{R}$ is given by

$$\mathbb{R} = (1+\gamma)\theta\mathbf{F}\cdot\mathbb{D}^{(1)}\cdot\mathbf{F}^\top + \mathbf{S}\otimes\mathbf{I}, \quad i.e.,$$

$$R_{ijkl} = (1+\gamma)\theta D^{(1)}_{irls}F_{jr}F_{ks} + S_{il}\delta_{jk}, \tag{3.18}$$

whereas the second-order tensors $\mathbf{H}$ and $\Delta\mathbf{V}$ are defined by

$$\mathbf{H} = 2\left(1+\gamma\right)\frac{\partial W^{(1)}}{\partial\mathbf{C}}\mathbf{F}^\top \tag{3.19}$$

and

$$\Delta\mathbf{V} = (\Delta\mathbf{Q})\mathbf{F}^\top. \tag{3.20}$$

Two special cases should be considered:
a. Damaging hyperelastic material with strain-energy function $W = (1+\bar{\delta})W^{(1)}$.
In the absence of viscous effects, $\tau_2 \to \infty$ and $\Delta\mathbf{V} = \mathbf{0}$. Hence

$$\mathbb{R} = \theta\mathbf{F}\cdot\mathbb{D}\cdot\mathbf{F}^\top + \mathbf{S}\otimes\mathbf{I}, \tag{3.21}$$

where $\mathbb{D} = 4\partial^2 W/(\partial\mathbf{C}\partial\mathbf{C})$, $\mathbf{S} = 2\theta\,\partial W/\partial\mathbf{C}$, and

$$\mathbf{H} = 2\frac{\partial W}{\partial\mathbf{C}}\mathbf{F}^\top \tag{3.22}$$

with $\Delta\mathbf{T}$ given by Eq. (3.17). In Perchikov et al. (2023) $\mathbf{T}$ was given by

$$\mathbf{T} = \theta\frac{\partial W}{\partial\mathbf{F}^\top}, \tag{3.23}$$

which provides $\mathbb{R} = \partial^2 W/(\partial\mathbf{F}\partial\mathbf{F}^\top)$ and $\mathbf{H} = \partial W/\partial\mathbf{F}^T$. By employing the identity: $\partial W/\partial\mathbf{F} = 2\mathbf{F}\partial W/\partial\mathbf{C}$, the expressions (3.21)–(3.22) can be recovered.
b. Viscoelastic material without damage.
Here, $\mathbb{R}$ is given by Eq. (3.18) with $\theta = 1$ and $\mathbf{S}$ by Eq. (3.2) with $\theta = 1$, and $\Delta\mathbf{T}$ is given by Eq. (3.17) with $\Delta\theta = 0$.

Returning to the case of viscoelastic material undergoing damage (with possible large local rotations), by defining the following two vectors:

$$\Delta\boldsymbol{\Sigma} = [\Delta T_{11}, \Delta T_{12}, \Delta T_{13}, \Delta T_{21}, \Delta T_{22}, \Delta T_{23}, \Delta T_{31}, \Delta T_{32}, \Delta T_{33}]$$

$$\Delta\boldsymbol{\Omega} = [\Delta F_{11}, \Delta F_{12}, \Delta F_{13}, \Delta F_{21}, \Delta F_{22}, \Delta F_{23}, \Delta F_{31}, \Delta F_{32}, \Delta F_{33}] \tag{3.24}$$

the incremental constitutive equations (3.17) can be written in matrix form:

$$\Delta\boldsymbol{\Sigma} = \mathbf{Z}\,\Delta\boldsymbol{\Omega} + \mathbf{H}\Delta\theta - \Delta\mathbf{V}, \tag{3.25}$$

where $\mathbf{Z}$ is the 9×9 tangent matrix (proportional to θ) of the material , which can be constructed from the 4th-order tangent tensor $\mathbb{R}$.

Finally, the incremental equations of equilibrium are:

$$\Delta T_{ij,i} = 0, \quad i, j = 1, 2, 3. \tag{3.26}$$

The (normalized) intact-matter mass-balance equation for the damaged material reads (see Perchikov et al. (2023)):

$$\theta\zeta - \nabla \cdot \mathbf{s} = 1, \tag{3.27}$$

where

$$\zeta = \exp\left[\left(\frac{W^{(1)}}{\phi}\right)^m\right] \tag{3.28}$$

and where $\phi > 0$ is a material parameter, related to material bond energy, and $m > 1$ is a numerical constant, related to the degree of localization of damage. In practice, to avoid numerical overflow, $(\zeta^{-1} + \epsilon)^{-1}$ is used instead of ζ, $\epsilon = 10^{-20}$ being a numerical constant. The quantity ζ^{-1} represents the statistically expected value of θ in the spatially homogeneous case (Perchikov et al. 2023). The incremental form of (-1 times) the mass balance equation then reads:

$$\frac{\partial\Delta s_1}{\partial X_1} + \frac{\partial\Delta s_2}{\partial X_2} + \frac{\partial\Delta s_3}{\partial X_3} - \frac{\Delta\theta}{\zeta^{-1} + \epsilon} - \frac{\theta}{(1 + \epsilon\zeta)^2}\Delta\zeta = 0 \tag{3.29}$$

with

$$\Delta\zeta = \frac{m}{\phi}\left(\frac{W^{(1)}}{\phi}\right)^{m-1}\zeta\;\Delta W^{(1)} \tag{3.30}$$

Last, we formulate the interfacial continuity conditions between two neighboring materials as:

$$[\![\Delta\mathbf{T}^\top]\!] \cdot \mathbf{N} = \mathbf{0}, \quad [\![\Delta\mathbf{u}]\!] = \mathbf{0}, \tag{3.31}$$

where $\mathbf{N}$ is a normal vector to the interface in the reference configuration and

$$[\![\Delta\mathbf{s}]\!] = \mathbf{0}, \quad [\![\Delta\theta]\!] = 0. \tag{3.32}$$

At this point, the hyperelastic potential has to be specified for the material. As in Perchikov et al. (2023), the modified Yeoh energy function (Volokh 2016) is employed here:

$$W^{(1)} = C_1\left(\hat{I}_1 - 3\right) + C_2\left(\hat{I}_1 - 3\right)^2 + \frac{K}{2}(J - 1)^2, \tag{3.33}$$

where $\hat{I}_1 = I_1/J^{2/3}$, $J = \det\mathbf{F}$, and C_1, C_2 and K are material constants.

Fig. 3 The response of the modified Yeoh viscoelastic material to various rates of applied uniaxial loading. Also shown is the corresponding response of the elastic material
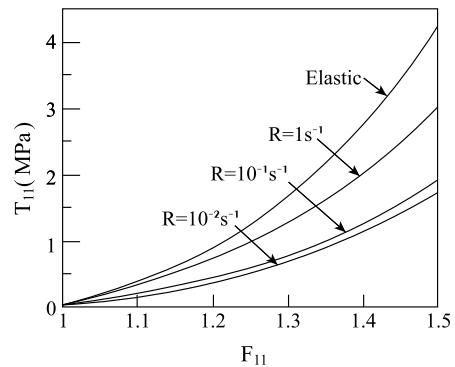
As in Perchikov et al. (2023), the following numerical values are used here: $C_1 = 0.617$ MPa, $C_2 = 1.215$ MPa, $K = 0.5$ GPa, $\phi = 0.1686$ MPa, $m = 3$ and $l = 0.1$ mm.

A noteworthy point concerns the way to determine the damage model parameters. As explaind in Perchikov et al. (2023), the topic is discussed in Volokh (2017) and in Faye et al. (2019). In principle, the parameters l and m describe the level of localization of damage and ϕ describes the bond energy density. In the present study, the value of ϕ was taken to be the same as in Abu-Qbeitah et al. (2022). The value of ϕ should be related to the values of C_1, C_2 in a manner that should be determined in comparison with experiments, as discussed in Faye et al. (2019). The localization parameters were chosen here from general considerations. In order to present inequilibrium-level localization, one has to take $m > 1$. The value $m = 2$ is already feasible, however, to check convergence a yet higher value should be checked. Noninteger values are also possible, but the dependence on m is not strong enough to justify it. The value of l should be significantly smaller than the computational element size (subcell length here). The typical element size in mechanical calculations is millimetric, hence the choice of $\bar{l}$ to be submillimetric is feasible. However, as shown in Volokh (2017), for some materials, the proper determination of material parameters consists in choosing an adequate, high-enough value of m, and then establishing l and ϕ by fitting to experimental data, such as a uniaxial-stress tension test up to global rupture of a specimen of proper size, for which the constants C_1, C_2 have been predetermined. As mentioned in Volokh (2017), the value of l can vary from 0.2 mm for rubber to 2.6 cm for concrete. When comparing a calculation based on the model with a test, l should fit the rupture thickness as observed, ϕ then to the rupture force (implicitly). As for m, it should determine temporal localization, i.e., time from onset to end of rupture in a quasistatic experiment (or a dynamic one, using the dynamic analysis, as discussed in Abu-Qbeitah et al. (2022)). Of course, m bears effect also on the level of spatial localization of the rupture zone, hence an appropriate value of l is expected for every adequate choice of m.

Figure 3 shows the response of the considered viscoelastic material specified by $\bar{\delta} = \frac{3}{2}$ and $\tau_2 = \frac{1}{4}s$. The figure shows the response of the viscoelastic material to uniaxial stress loading applied at rates of $R = 1/s, 0.1/s$ and $0.01/s$. Application of the loading at a lower rate does not appreciably change the material response. Also shown in the figure is the response of the elastic material, in which $\tau_2 \to \infty$. All the results presented in this article were generated with the applied rate of $R = \frac{1}{100s}, \bar{\delta} = \frac{3}{2}$ and $\tau_2 = \frac{1}{4}s$.

Zero-dimensional analysis. It is illustrative to make a zero-dimensional model of a degrading viscoelastic composite and to observe the associated response. To this end, we assume a parallel construction of solid heperelastic material, modeled by a spring, in which

Fig. 4 The stress response for the elastic (solid) and viscoelastic (dash) case for a zero-dimensional model of a composite with a hyperelastic phase and a degrading viscoelastic phase, with the intact-material mass fraction history (indistinguishable in the two cases) in the inset
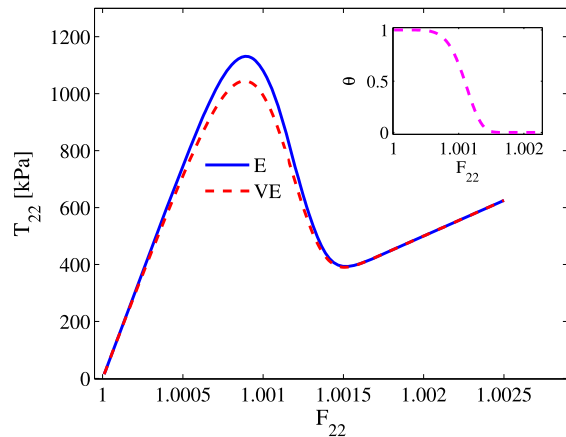
damage does not develop, and a piece of viscoelastic degrading material, of the sort described in Sect. 2, modeled by a construction, as shown in Fig. 2. We assume this structure could qualitatively approximate a composite comprised of a hyperelastic phase and a viscoelastic degrading phase. We assume uniaxial strain applied with a constant strain rate as specified above and material properties as listed above. The corresponding (homogeneous) solution for the intact-material mass fraction and for the viscoelastic and elastic-case stress would be as follows:

$$\theta_{0D} \approx e^{-\alpha t^6}, \ \bar{\alpha} \triangleq \left[\frac{(1+\bar{\delta})\left(K + \frac{8}{3}C_1\right)}{\phi} \right]^m R^{2m} \approx 407530 \ \text{sec}^{-6}, \ F_{22} = 1 + Rt$$

$$T_{22}^{(E)} \approx \frac{1}{2}\left(K + \frac{8}{3}C_1\right)Rt + \left(K + \frac{8}{3}C_1\right)Rte^{-\bar{\alpha}t^6} + \bar{\delta}\left(K + \frac{8}{3}C_1\right)Rte^{-\alpha t^6}$$

$$T_{22}^{(VE)} \approx \frac{1}{2}\left(K + \frac{8}{3}C_1\right)Rt + \left(K + \frac{8}{3}C_1\right)Rte^{-\bar{\alpha}t^6}$$

$$+ \bar{\delta}\left(K + \frac{8}{3}C_1\right)R\tau_2 e^{-\bar{\alpha}t^6}\left(1 - e^{-t/\tau_2}\right),$$

(3.34)

where the first term (linear in time) represents the elastic, nondegrading spring mimicking the constant part of the composite (arbitrarily taken here to be of half the initial stiffness of the viscoelastic degrading material).

The stress for both cases is plotted in Fig. 4, with the θ profile given in the inset. One observes that the viscoelastic case shows smaller maximum stress, which can be attributed to the fact that for slow loading, not all the applied strain goes to the spring, some goes to the dashpot. Consequently, the stress in the spring connected in queue to the dashpot is smaller than for the elastic case, where the dashpot is locked, preventing viscous flow.

4 Finite strain viscoelastic micromechanical analysis

In the present section, the finite strain HFGMC micromechanical analysis for the prediction of the response of viscoelastic composites in which one or several constituents are viscoelastic, with behavior as has been presented in Sect. 2, is discussed. To this end, consider
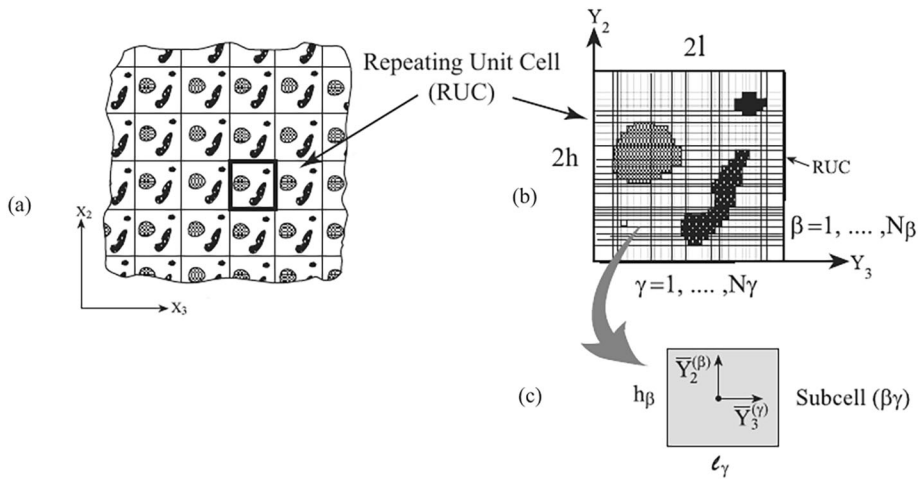
Fig. 5 (a) Doubly-periodic composite, defined with respect to global initial coordinates (X_1, X_2, X_3) (note a similar figure in Perchikov et al. (2023)). (b) The RUC, represented with respect to local initial coordinates (Y_1, Y_2, Y_3), divided into N_β and N_γ subcells, in the Y_2 and Y_3 directions, respectively. (c) A characteristic subcell $(\beta\gamma)$ with initial local coordinates $\bar{Y}_2^{(\beta)}$ and $\bar{Y}_3^{(\gamma)}$ with origin located at the center

a multiphase composite whose microstructure is distributed in a *doubly* periodic manner, as shown in Fig. 5(a). The composite is described with respect to a global initial system of coordinates (X_1, X_2, X_3). Figure 5(b) shows the RUC, defined with respect to local initial coordinates (Y_2, Y_3), of the periodic composite. Herein, the finite strain HFGMC micromechanical model is employed to predict the behavior of the composite caused by the application of external mechanical loading. The rectangular RUC of the composite is divided into N_β and N_γ subcells in the Y_2 and Y_3 directions, respectively. Each subcell is labeled by the indices $(\beta\gamma)$ with $\beta = 1, \ldots, N_\beta$ and $\gamma = 1, \ldots, N_\gamma$. The dimensions of subcell $(\beta\gamma)$ in the Y_2 and Y_3 directions are denoted by h_β and l_γ, respectively. A local coordinate system $(\bar{Y}_2^{(\beta)}, \bar{Y}_3^{(\gamma)})$ is introduced in each subcell, whose origin is located at its center, see Fig. 5(c).

In the framework of the finite strain HFGMC analysis, which is presently employed to predict the behavior of the considered composites, the increments of the mechanical displacements $\Delta \mathbf{u}^{(\beta\gamma)}$ in the subcell $(\beta\gamma)$ are expanded in terms of special second-order polynomials. To this end, let the vector $\Delta \mathbf{W}^{(\beta\gamma)}$ represent the components of the displacement vector $\Delta \mathbf{u}^{(\beta\gamma)}$:

$$\Delta \mathbf{W}^{(\beta\gamma)} = [\Delta u_1, \Delta u_2, \Delta u_3]^{(\beta\gamma)}. \tag{4.1}$$

The 2nd-order expansion is given by

$$\Delta \mathbf{W}^{(\beta\gamma)} = \Delta \bar{\mathbf{W}} + \Delta \mathbf{W}_{(00)}^{(\beta\gamma)} + \bar{Y}_2^{(\beta)} \Delta \mathbf{W}_{(10)}^{(\beta\gamma)} + \bar{Y}_3^{(\gamma)} \Delta \mathbf{W}_{(01)}^{(\beta\gamma)}$$
$$+ \frac{1}{2} \left(3\bar{Y}_2^{(\beta)2} - \frac{h_\beta^2}{4} \right) \Delta \mathbf{W}_{(20)}^{(\beta\gamma)} + \frac{1}{2} \left(3\bar{Y}_3^{(\gamma)2} - \frac{l_\gamma^2}{4} \right) \Delta \mathbf{W}_{(02)}^{(\beta\gamma)}, \tag{4.2}$$

where $\Delta \bar{\mathbf{W}} = [\Delta \bar{\mathbf{F}} \cdot \mathbf{X}]$ consists of the externally applied loading.

Similarly,

$$\Delta\theta^{(\beta\gamma)} = \Delta\theta^{(\beta\gamma)}_{(00)} + \bar{Y}_2^{(\beta)}\Delta\theta^{(\beta\gamma)}_{(10)} + \bar{Y}_3^{(\gamma)}\Delta\theta^{(\beta\gamma)}_{(01)}$$

$$+ \frac{1}{2}\left(3\bar{Y}_2^{(\beta)2} - \frac{h_\beta^2}{4}\right)\Delta\theta^{(\beta\gamma)}_{(20)} + \frac{1}{2}\left(3\bar{Y}_3^{(\gamma)2} - \frac{l_\gamma^2}{4}\right)\Delta\theta^{(\beta\gamma)}_{(02)}. \tag{4.3}$$

The unknown coefficients $\Delta\mathbf{W}^{(\beta\gamma)}_{(mn)}$ and $\Delta\theta^{(\beta\gamma)}_{(mn)}$ are determined, as shown in Appendix B, by implementing the equilibrium equations (3.26) and the intact-material mass balance equation (3.27) together with the interfacial continuity conditions (3.31)–(3.32), and periodic conditions, which are discussed as follows.

In the framework of the HFGMC micromechanical analysis, periodic boundary conditions must be imposed to ensure the periodic microstructure character of the composite, as represented by the repeating unit cell of Fig. 5(b). These conditions require that the increments of the displacement vectors $\mathbf{u}$ and the traction vectors $\mathbf{T}^{\mathbf{N}} = \mathbf{T}^\top \cdot \mathbf{N}$ at the opposite edges of the repeating unit cell are identical. These imply that:

$$\Delta\mathbf{u}(Y_2 = 0) = \Delta\mathbf{u}(Y_2 = 2h), \quad \Delta\mathbf{T}^{\mathbf{N}}(Y_2 = 0) = \Delta\mathbf{T}^{\mathbf{N}}(Y_2 = 2h),$$

$$\Delta\mathbf{u}(Y_3 = 0) = \Delta\mathbf{u}(Y_3 = 2l), \quad \Delta\mathbf{T}^{\mathbf{N}}(Y_3 = 0) = \Delta\mathbf{T}^{\mathbf{N}}(Y_3 = 2l). \tag{4.4}$$

Similarly,

$$\Delta\theta(Y_2 = 0) = \Delta\theta(Y_2 = 2h), \quad \Delta s_2(Y_2 = 0) = \Delta s_2(Y_2 = 2h),$$

$$\Delta\theta(Y_3 = 0) = \Delta\theta(Y_3 = 2l), \quad \Delta s_3(Y_3 = 0) = \Delta s_3(Y_3 = 2l). \tag{4.5}$$

The micromechanical analysis results in an equation that expresses the increments of the stress $\Delta\mathbf{T}$ and the mass flux $\Delta\mathbf{s}$ in terms of increments of the displacements $\Delta\mathbf{U}$ and intact material mass fraction $\Delta\theta$, see Eq. (B.29), which can be represented as follows:

$$\left\{\begin{matrix}\Delta\mathbf{T}\\\Delta\mathbf{s}\end{matrix}\right\}^{(\beta\gamma)} = \begin{bmatrix}\mathbf{K}_{11} & \mathbf{K}_{12}\\\mathbf{K}_{21} & \mathbf{K}_{22}\end{bmatrix}^{(\beta\gamma)}\left\{\begin{matrix}\Delta\mathbf{U}\\\Delta\theta\end{matrix}\right\}^{(\beta\gamma)} + \left\{\begin{matrix}\Delta\boldsymbol{\Phi} - \Delta\mathbf{V}\\\mathbf{0}\end{matrix}\right\}^{(\beta\gamma)}, \tag{4.6}$$

where $\Delta\boldsymbol{\Phi}$ are expressions that involve the applied far-field.

5 The method of solution

As discussed in Perchikov et al. (2023), the following predictor-corrector approach should be implemented to obtain a convergent solution of the coupled system of mechanical-equilibrium–intact-mass-density-balance equations (the relation to the staggered method of Miehe et al. (2010) is given in Perchikov et al. (2023)). This results in the following three-steps predictor-corrector problems, solved consecutively.

Problem I: Here, the following modified relations are used instead of Eq. (4.6):

$$\left\{\begin{matrix}\Delta\mathbf{T}\\\Delta\mathbf{s}\end{matrix}\right\}^{(\beta\gamma)} = \begin{bmatrix}\mathbf{K}_{11} & \mathbf{0}\\\mathbf{0} & \mathbf{K}_{22}\end{bmatrix}^{(\beta\gamma)}\left\{\begin{matrix}\Delta\hat{\mathbf{U}}_*\\\Delta\boldsymbol{\theta}_\circ\end{matrix}\right\}^{(\beta\gamma)} + \left\{\begin{matrix}\Delta\boldsymbol{\Phi} - \Delta\mathbf{V}\\\mathbf{0}\end{matrix}\right\}^{(\beta\gamma)}. \tag{5.1}$$

The implementation of the continuity of displacements and tractions between the subcells and the periodicity conditions, namely, Eqs. (B.32)–(B.35), results in a global system of equations, which provides $\Delta\hat{\mathbf{U}}^{(\beta\gamma)}_*$ in all the subcells.

Problem II: In the framework of this problem, Eq. (4.6) is modified to include the established increments $\Delta\hat{\mathbf{U}}_*^{(\beta\gamma)}$, as follows:

$$\left\{ \begin{array}{c} \Delta\mathbf{T} \\ \Delta\mathbf{s} \end{array} \right\}^{(\beta\gamma)} = \left[\begin{array}{cc} \mathbf{K}_{11} & \mathbf{0} \\ \mathbf{0} & \mathbf{K}_{22} \end{array} \right]^{(\beta\gamma)} \left\{ \begin{array}{c} \Delta\hat{\mathbf{U}}_\circ \\ \Delta\boldsymbol{\theta}_* \end{array} \right\}^{(\beta\gamma)} + \left\{ \begin{array}{c} \mathbf{0} \\ \mathbf{K}_{21}\Delta\hat{\mathbf{U}}_* \end{array} \right\}^{(\beta\gamma)}. \tag{5.2}$$

By implementing the continuity and periodicity conditions (B.32)–(B.35), the solution of the resulting global equations yields $\Delta\boldsymbol{\theta}^{(\beta\gamma)} = \Delta\boldsymbol{\theta}_*^{(\beta\gamma)}$ in all subcells. Consequently, the mass fractions in all subcells can be updated according to

$$\boldsymbol{\theta}^{(\beta\gamma)} = \boldsymbol{\theta}_{\text{previous}}^{(\beta\gamma)} + \Delta\boldsymbol{\theta}_*^{(\beta\gamma)}, \tag{5.3}$$

where $\boldsymbol{\theta}_{\text{previous}}^{(\beta\gamma)}$ are the intact-material mass fractions that were computed at the previous applied loading increment.

Problem III: With the computed mass densities $\boldsymbol{\theta}^{(\beta\gamma)}$ in all subcells, the following modification of Eq. (4.6) is used:

$$\left\{ \begin{array}{c} \Delta\mathbf{T} \\ \Delta\mathbf{s} \end{array} \right\}^{(\beta\gamma)} = \left[\begin{array}{cc} \mathbf{K}_{11} & \mathbf{0} \\ \mathbf{0} & \mathbf{K}_{22} \end{array} \right]^{(\beta\gamma)} \left\{ \begin{array}{c} \Delta\mathbf{U} \\ \Delta\boldsymbol{\theta}_{\circ\circ} \end{array} \right\}^{(\beta\gamma)} + \left\{ \begin{array}{c} \Delta\boldsymbol{\Phi} - \Delta\mathbf{V} + \mathbf{K}_{12}\Delta\boldsymbol{\theta}_* \\ \mathbf{0} \end{array} \right\}^{(\beta\gamma)}. \tag{5.4}$$

The implementation of the continuity and periodicity conditions (B.32)–(B.35) yields a global equation whose solution provides $\Delta\mathbf{U}^{(\beta\gamma)}$ in all subcells. Hence

$$\mathbf{U}^{(\beta\gamma)} = \mathbf{U}_{\text{previous}}^{(\beta\gamma)} + \Delta\mathbf{U}^{(\beta\gamma)}. \tag{5.5}$$

From Eq. (B.28) it is evident that the mechanical and mass fraction increments $\Delta W_{mn}^{(\beta\gamma)}$ and $\Delta\theta_{mn}^{(\beta\gamma)}$; $m = n = 0, 1, 2$ can be considered determined in all subcells (the quantities with subscript $\circ$ and $\circ\circ$ are not to be used after the solution of the associated linear system).

6 Applications

Consider the modified Yeoh (MY) energy function given by Eq. (3.33). As discussed, the chosen parameters are $\bar{\delta} = 3/2$ and $\tau_2 = 0.25s$. Results have been obtained by specifying the size of the RUC as $2h = 2l = 1$ mm, which is divided into $N_\beta = N_\gamma = 100$ subcells. All the field distributions that are shown in the following have been recorded at the first occurrence of $\theta_{\min} < 0.01$.

For the applications discussed herein an in-house program developed by the authors was used for the solution of the viscoelastic damage problem for the chosen composites. The program was implemented in Fortran, using the free Unix-Intel compiler, and ran on a local university processor.

As a first application, consider porous material, the solid part of which is rank-1 generalized Maxwell viscoelastic with a hyperelastic limit characterized by the MY functional. We assume circular holes, see the corresponding RUC in Fig. 6. The volume fraction of the holes (porosity) is $v_f = 0.05$. The porous material is stretched by applying incrementally a far-field loading $\bar{F}_{22}$ at a rate of R = 0.01/s. The resulting nonlinear variation of the first Piola-Kirchhoff stress averaged over all subcells, $\bar{T}_{22}$, is shown in Fig. 6(a) for the considered viscoelastic (VE) porous materials and compared with the corresponding elastic (E) response ($\tau_2 \to \infty$). Figure 6(b) shows the decrease of the spatial minimum of the intact
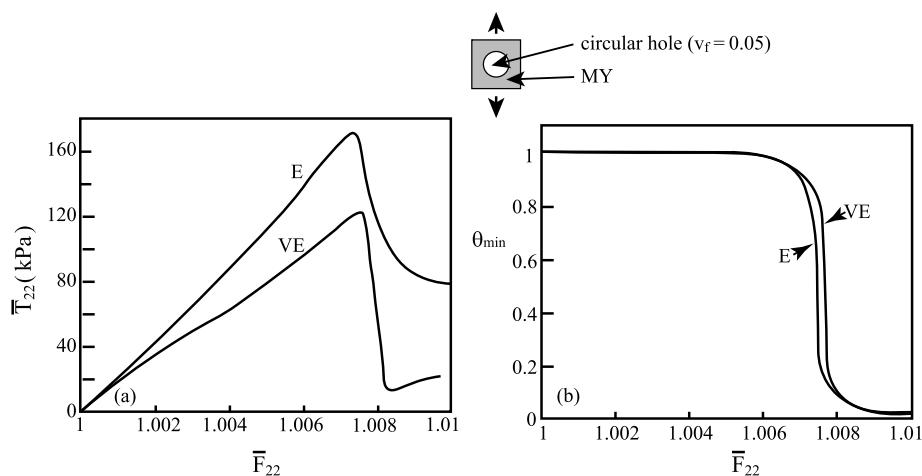
Fig. 6 Porous MY material of $v_f = 0.05$ porosity. (a) Comparison between the variations of the global response $\bar{T}_{22} - \bar{F}_{22}$ of the viscoelastic and elastic porous materials. (b) Comparison between the variations of $\theta_{\min} - \bar{F}_{22}$ of the viscoelastic and elastic porous materials

material ratio θ with the applied loading in the viscoelastic and elastic porous materials. The delay of total fracture caused by the viscous effects can be well observed.

The distributions of the deformation gradient F_{22}, the stress T_{22} (kPa) and the mass fraction θ in the RUC for the viscoelastic case are shown in Fig. 7(a), (c) and (e), respectively. The corresponding distributions in the elastic case are displayed in Fig. 7(b), (d) and (f).

The deformation gradient in the viscoelastic case varies between about 9% tension and 6% compression. The maximum value of the stress is 600 kPa, whereas its maximum average value is about 120 kPa. The elastic case, on the other hand, exhibits higher strain. Here too a higher value of tensile stress (local – 700 kPa, average – 170 kPa) can be observed. The mass fraction θ distribution exhibits the material weakening around the hole with its maximum values loci aligning in the X_3-direction. The zones where $\theta \approx 0$ indicate the locations of material separation (cracks), while low nonzero values indicate where the material-weakening diffusion takes place. The comparisons between the viscoelastic and elastic distributions in all cases show that the viscous effect decreases the extension of the damaged region in the composite.

Figures 8 and 9 exhibit the corresponding behaviors and field distributions when the porosity is increased to $v_f = 0.1$.

Here, too, the spread of damage is more pronounced in the elastic case.

The next application investigates failure evolution in fiber-reinforced soft (degrading) matrix composites. To this end, the Blatz ond Ko (BK) material, Blatz and Ko (1962), is chosen to represent the hyperelastic strain energy function of the fibers. It is given by:

$$W = \frac{\mu}{2}\left(\frac{I_2}{I_3} + 2\sqrt{I_3} - 5\right), \tag{6.1}$$

where $\mu = 0.22$ MPa.

In the following, the response of a fiber-reinforced composite comprised of BK continuous fibers reinforcing a degrading viscoelastic MY matrix is considered. Figure 10 shows the comparisons between the average stress $\bar{T}_{22}$ response and $\theta_{\min}$ history as obtained in the case of a viscoelastic and an elastic MY matrix where the fiber volume ratio is $v_f = 0.05$.
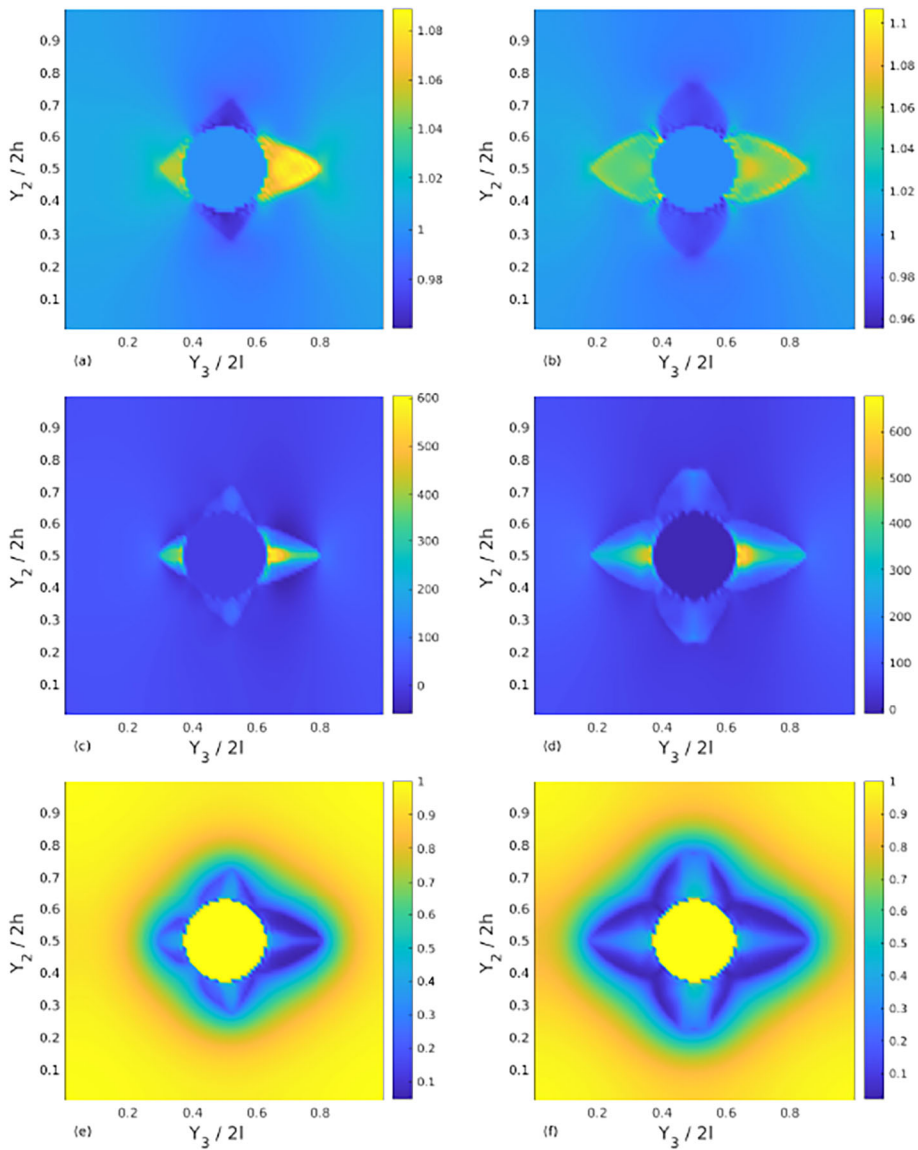
Fig. 7 Porous viscoelastic MY material of $v_f = 0.05$ porosity. (a), (c), (e) The distributions of the deformation gradient F_{22}, the stress T_{22} (kPa), and mass fraction θ, respectively. (b), (d), (f) The corresponding distributions in the elastic case ($\tau_2 \to \infty$)

The effect of the reinforcing fibers can be observed by comparison with Fig. 6 of the porous material, revealing stress increase caused by the presence of the fibers. Comparison of the $\theta_{\min}$ curves between Figs. 10(b) and 6(b) shows that the reinforcement slightly delays, as expected, the occurrence of failure. As to the field distributions in the present case of a viscoelastic BK/MY composite, those are exhibited in Fig. 11.
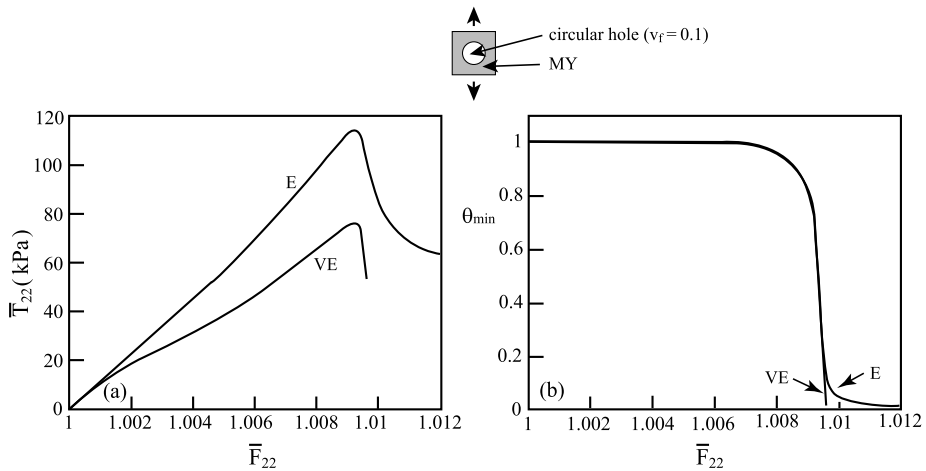
Fig. 8 Porous MY material of $v_f = 0.1$ porosity. (a) Comparison between the variations of the global response $\bar{T}_{22} - \bar{F}_{22}$ of the viscoelastic and elastic porous materials. (b) Comparison between the variations of $\theta_{\min} - \bar{F}_{22}$ of the viscoelastic and elastic porous materials

Figure 11(a) exhibits significant deformation of the composite, reaching about 100% strain, compared to about 30% in the elastic case. The stress T_{22}, as shown in Fig. 11(b), approaches 1.4 MPa. Within the fibers, on the other hand, a compressive stress of about 50 kPa is attained. The stress variation in the elastic case is more moderate in comparison. Figure 11(c) exhibits the existence of cracks in locations where $\theta \approx 0$ and weakened diffused regions characterized by $\theta < 1$.

Figures 12 and 13 exhibit the corresponding behavior of a fiber-reinforced BK/MY composite as discussed above but with a fiber volume fraction of $v_f = 0.1$.

As expected, the increase in the amount of reinforcement seems to decrease the deformation and tensile stresses, while increasing the compressive stress in the fibers to about 100 kPa.

Thus far, the far-field loading was applied in the transverse X_2-direction. It should be interesting to compare the resulting effective response of the composite to other types of loading. To this end, consider the BK/MY fiber-reinforced viscoelastic composite with the fiber volume fraction of $v_f = 0.1$. Figure 14 exhibits the comparison between the $\bar{T}_{22} - \bar{F}_{22}$ responses and the $\theta_{\min} - \bar{F}_{22}$ histories corresponding to the application of three types of loading, as indicated in the following.

The profiles of the response to loading in the transverse X_2-direction, and bi-axial same-sign loading in the X_2 and X_3 transverse directions are compared to the profiles of the response to the simultaneous application of tensile and compressive loading in the X_2 and X_3 transverse directions, respectively. Figure 14 shows that the application of tensile and compressive loading in the transverse directions significantly delays the initial onset of damage in the composite. Similarly, the occurrence of damage in the composite caused by the application of uni-axial loading is delayed compared to the onset of damage for the bi-axial loading case.

In the aforementioned applications, the considered composites possess square symmetry, as a result of which the effective behavior is not isotropic in the transverse directions. Overall nearly trasversely isotropic behavior of fiber-reinforced composites is obtained by considering hexagonal arrays of fiber distributions in the reinforced matrix. To this end, con-
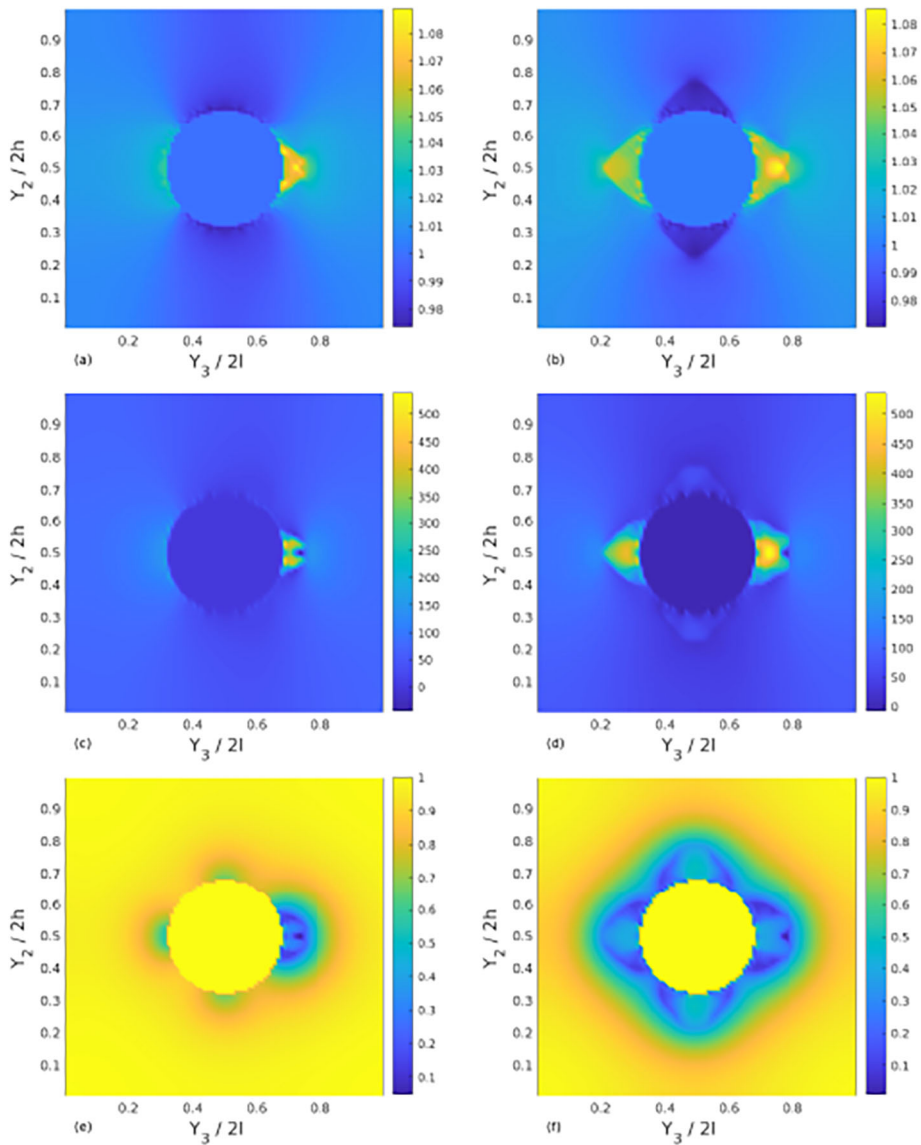
Fig. 9 Porous viscoelastic MY material of $v_f = 0.1$ porosity. (a), (c), (e) The distributions of the deformation gradient F_{22}, the stress T_{22} (kPa), and mass fraction θ, respectively. (b), (d), (f) The corresponding distributions in the elastic case ($\tau_2 \to \infty$)

sider a BK/MY fiber-reinforced composite ($v_f = 0.1$), in which the distributed fibers form a hexagonal array inside the MY matrix. Figure 15 shows the RUC of the composite and the resulting elastic and viscoelastic average responses $\bar{T}_{22} - \bar{F}_{22}$, as well as $\theta_{\min} - \bar{F}_{22}$ histories. Comparison of this figure with Fig. 12 shows the negligible effect of the difference between hexagonal and square symmetries in the fiber distributions in the composite.

Conversely, comparison of Figs. 13 and 16 shows the appreciably different field distributions obtained for the two cases.
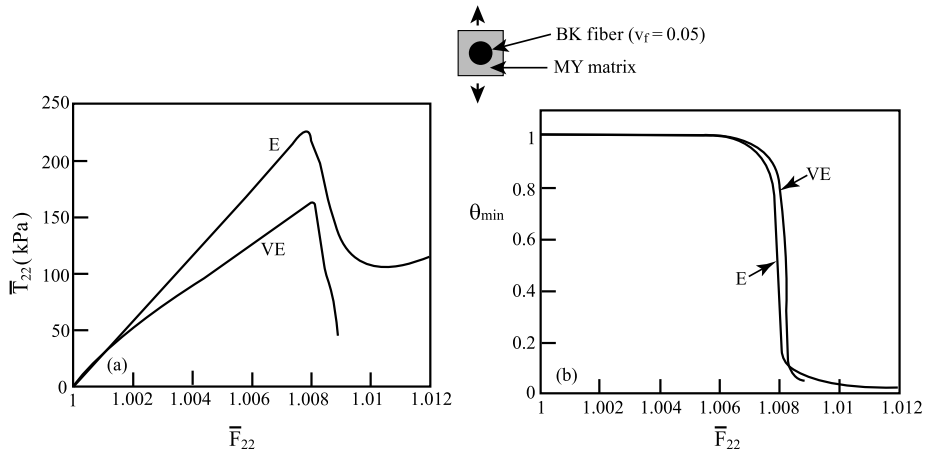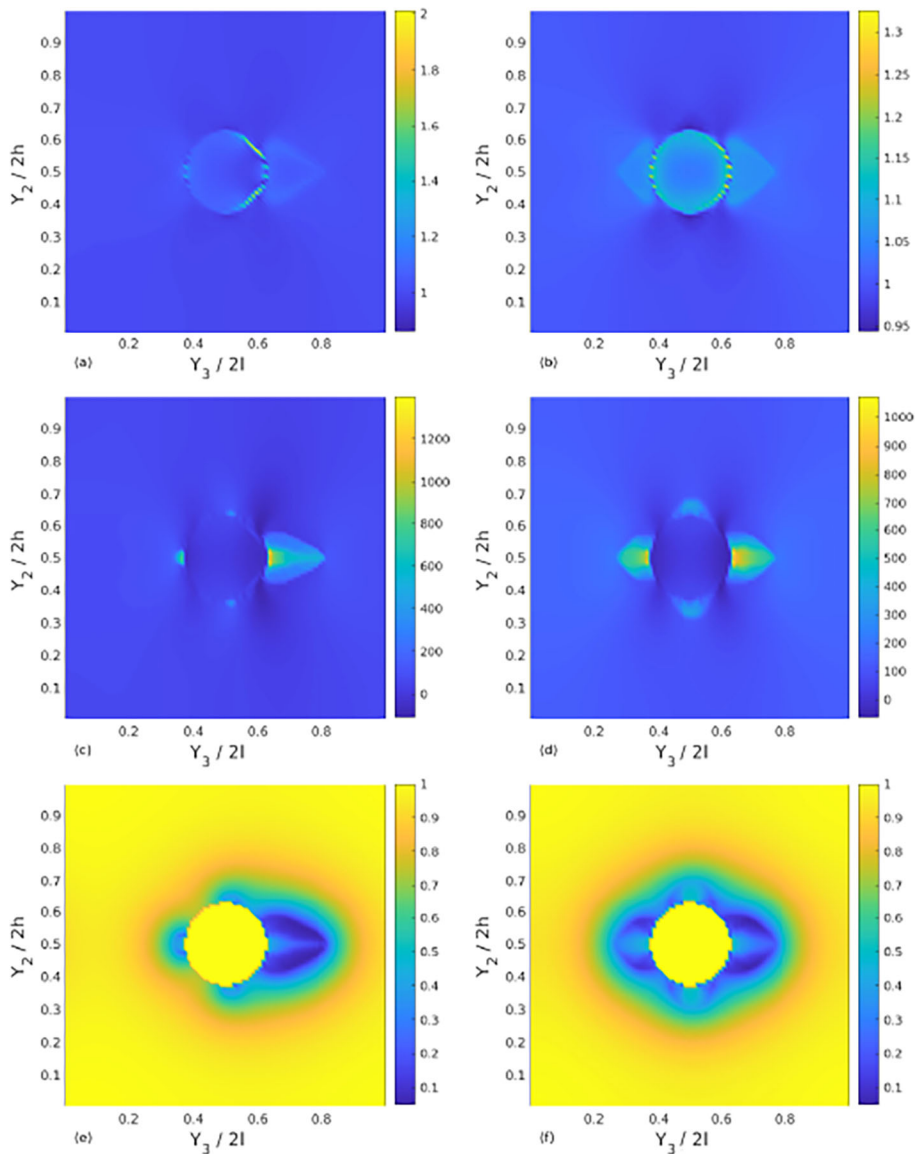
Fig. 10 BK/MY composite material with a fiber volume fraction of $v_f = 0.05$. (a) Comparison between the variations of the global response $\bar{T}_{22} - \bar{F}_{22}$ of the viscoelastic and elastic composite materials. (b) Comparison between the variations of $\theta_{\min} - \bar{F}_{22}$ of the viscoelastic and elastic composite materials

In the final application, a BK/MY fiber-reinforced composite with a fiber volume fraction of $v_f = 0.1$ is considered, in which the fibers are randomly distributed in the matrix. The resulting viscoelastic and elastic $\bar{T}_{22} - \bar{F}_{22}$ responses are shown in Fig. 17, along with the $\theta_{\min} - \bar{F}_{22}$ plots.

Comparison of this figure with Fig. 12 shows an increase in the average stresses and a damage-onset delay caused by the randomization effect. The corresponding field distributions are presented in Fig. 18.

Concerning the meaning of a random pattern in the RUC in periodic composites, we refer the reader to the relevant discussion in Perchikov et al. (2023), which we partially reproduce here. One might wonder regarding the adequacy of periodic boundary conditions for the case of a random pattern of inclusions in a matrix. Periodic boundary conditions imply that the distribution of the stress and damage fields inside a representative unit cell is expected to be the same for all the cells. This can only hold if the cells have identical distribution of fibers, even if it is a random one. The present approach is designed specifically for the analysis of periodic composites, not random ones. Thus, it is not opted here to analyze an infinite span of random composite matter. Instead, it is assumed that the material is periodic, with identical cells, where the representative cell has a random distribution of inclusions, perhaps as a result of some topology optimization procedure for desired response, and the representative cells are glued to a periodic pattern. In such a setting, the fibers will be of non-circular cross-section at the boundaries of the unit cells. Moreover, the adhesive layers required for practical implementations are neglected here. It is also possible to maintain the picture of right fibers by modeling only a quarter of the RUC as random and reflecting it in both directions. However, the level of randomness of that pattern will be smaller than of the chosen pattern. It is also possible to position all the inclusions well inside the unit cell, to prevent an inclusion from having a non-circular cross section, however it is only crucial for rigid authentic fibers, such as those made of carbon or glass. In the examined case the inclusion modeled by a BK material was needed only to model a different phase, with no damage accumulation, and the circular cross-section is not a rigid requirement. A random unit cell made with BK fibers can be cut from a larger random pattern, with some fibers cut

Fig. 11 BK/MY viscoelastic composite material with a fiber volume fraction of $v_f = 0.05$. (a), (c), (e) The distributions of the deformation gradient F_{22}, the stress T_{22} (kPa), and intact-material mass fraction θ, respectively. (b), (d), (f) The corresponding distributions in the elastic case ($\tau_2 \to \infty$)

in the middle. Then, a periodic pattern can be constructed from gluing the unit cells together. With some fibers cut in the middle, an even more random pattern is reproduced, albeit with periodicity on the macro-scale. The main point in the analysis of the random pattern is in any case to observe the spontaneous localization of damage based on the intricacies of nontrivial stress localization geometry.
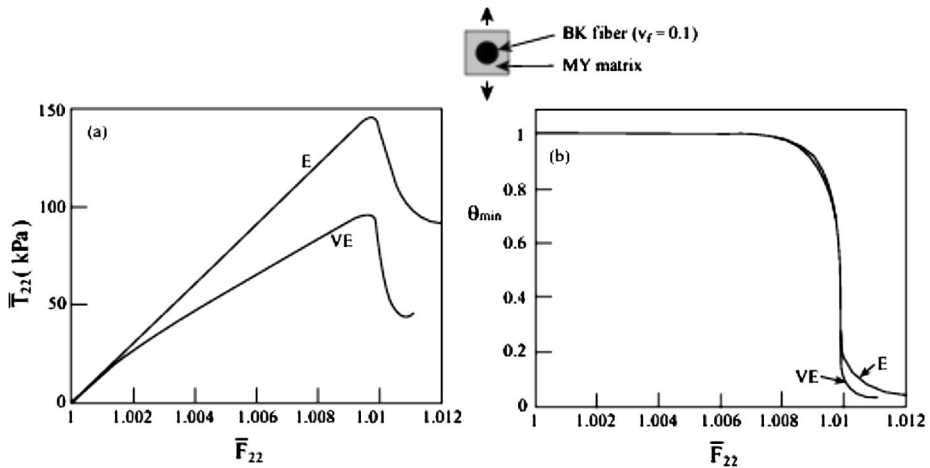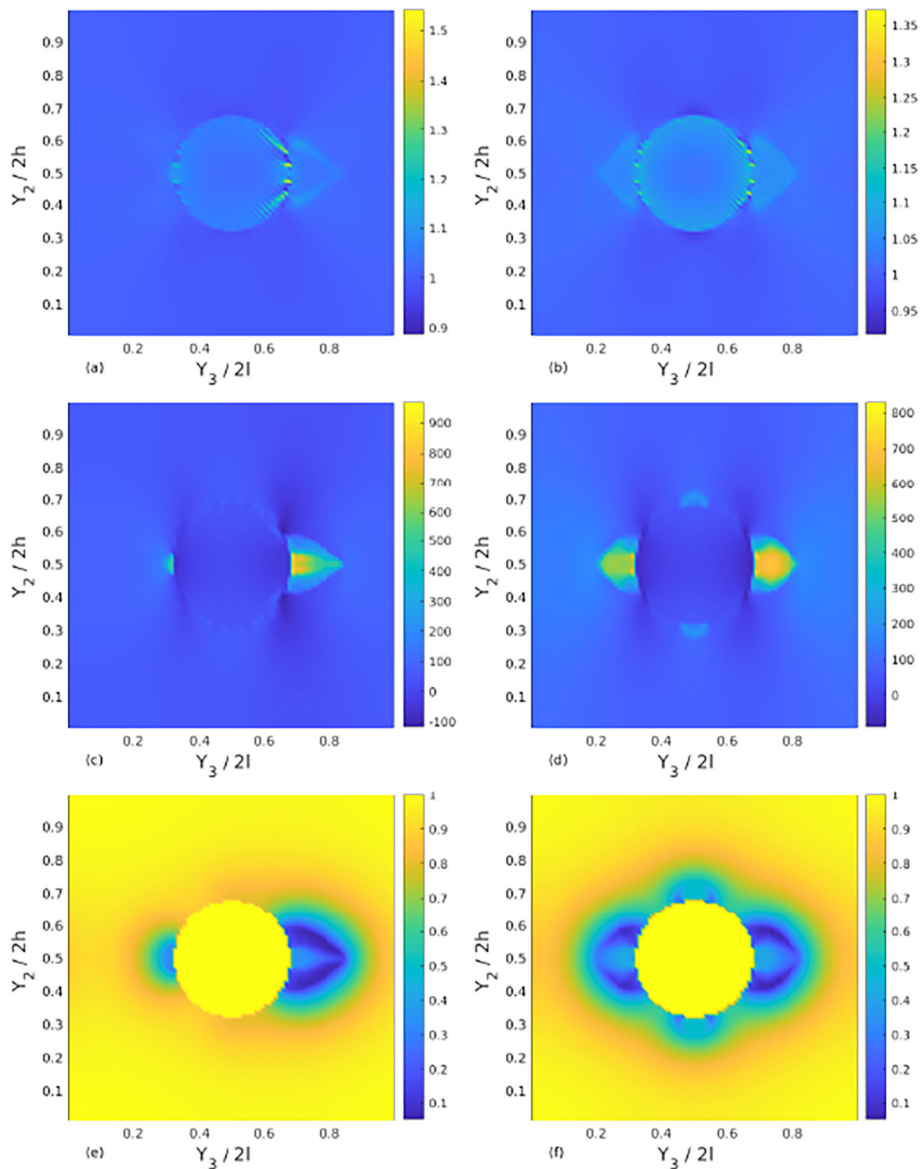
Fig. 12 BK/MY composite material with a fiber volume fraction of $v_f = 0.1$. (a) Comparison between the variations of the global response $\bar{T}_{22} - \bar{F}_{22}$ of the viscoelastic and elastic composite materials. (b) Comparison between the variations of $\theta_{\min} - \bar{F}_{22}$ of the viscoelastic and elastic composite materials

For further details on the issue of the validity of representing a random medium by a two-scale construction with a periodic arrangement of RUCs, in each of which a random arrangement of fibers is introduced, we refer the reader to Murthy et al., where it is also shown that the effective properties of the former do in fact converge to those of the latter. Moreover, the micromechanical fields are also approximated well by the aforementioned construction. In what concerns the approximation of biological tissues by composite material models with discrete phases, we refer the reader to Breiman et al. (2020), where such approximations were validated. In general, both for the purpose of establishing effective properties and critical local field values, at least in quasistatic loading, modeling complex media relying on simplified seemingly discrete rheological models has been proven successful (Simo and Hughes 1998).

Concerning the question of the stability of a periodic damage pattern in a periodic composite, we also refer the reader to Perchikov et al. (2023).

7 Conclusions

In the present investigation, the coupled equilibrium and intact-material mass balance equations incorporating a viscoelastic rheological constitutive model have been integrated with the finite strain HFGMC micromechanics in order to predict the evolution of damage in porous soft materials and fiber-reinforced soft-matrix periodic composites subjected to a far-field loading. The employed finite-strain viscoelastic constitutive material equations are based on a convolution-integral representation in conjunction with an arbitrary chosen hyperelastic energy function. This micromechanical analysis yields a large sparse system of algebraic equations. In order to establish a convergent solution, a predictor-corrector algorithm is employed, providing the field variables in all points in the RUC of a soft-matrix composite material with doubly periodic microstructure. The composite's response and damage evolution can be readily determined from the established field variables.

Fig. 13 BK/MY viscoelastic composite material with a fiber volume fraction of $v_f = 0.1$. (a), (c), (e) The distributions of the deformation gradient F_{22}, the stress T_{22} (kPa), and intact-material mass fraction θ, respectively. (b), (d), (f) The corresponding distributions in the elastic case ($\tau_2 \to \infty$)

Although the 1d Zener model was employed here, the generalization to Maxwell's model of any degree is straightforward. Moreover, the presently chosen finite strain viscoelastic model belongs to a class referred to as finite linear viscoelasticity, c.f. Holzapfel (2000), in which the deformations (rotations) may be large, but the deviations from the equilibrium state are small. In the framework of finite viscoelasticity, however, both deformations and deviations from equilibrium may be large. The present investigation can be generalized to
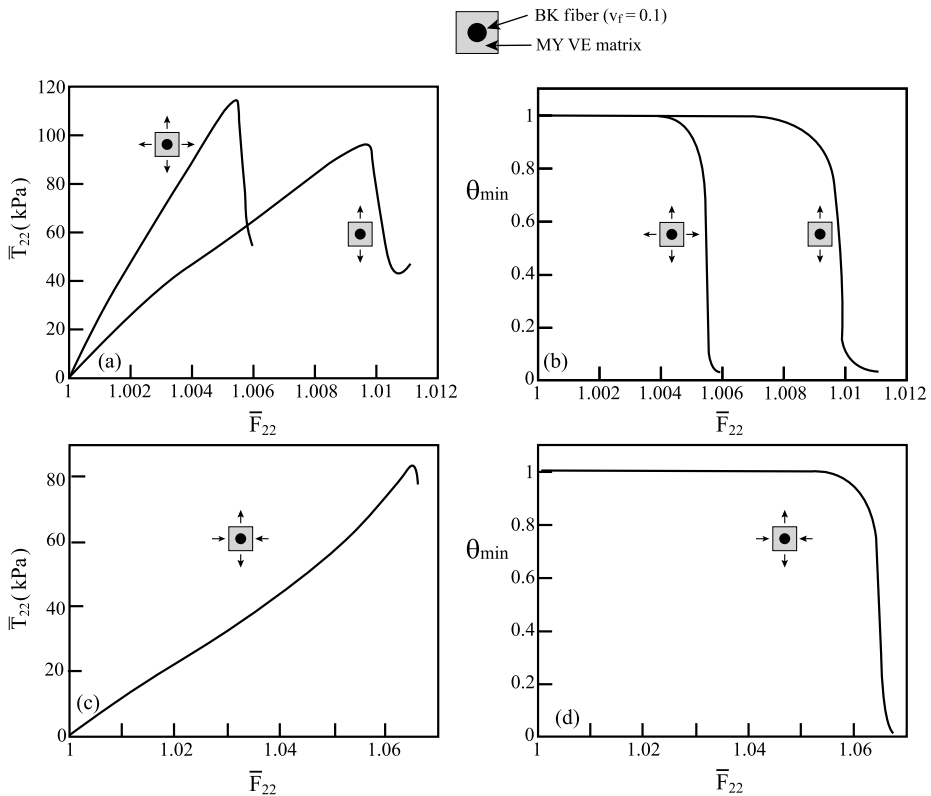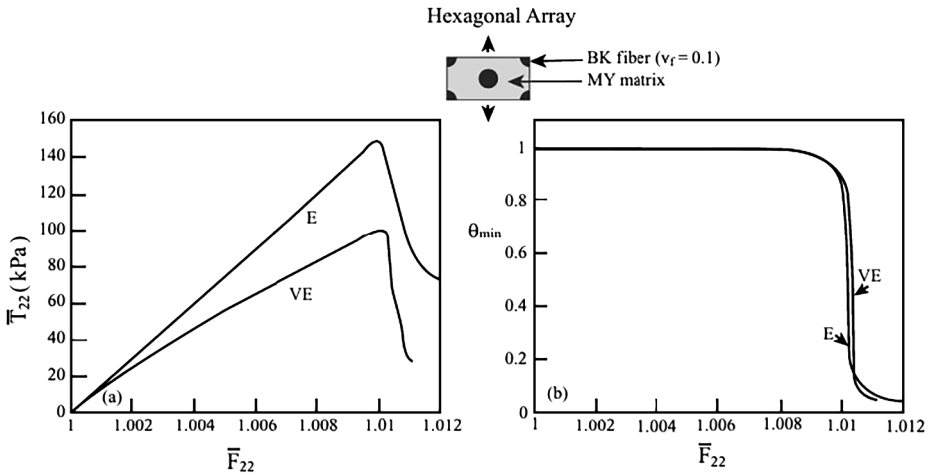
Fig. 14 BK/MY viscoelastic composite material with a fiber volume fraction of $v_f = 0.1$. (a) Comparison between the variations of the global response $\bar{T}_{22} - \bar{F}_{22}$ of the composite material with two different types of loading. (b) Comparison between the variations of $\theta_{min} - \bar{F}_{22}$ of the composite material with two different types of loading. (c) The variation of the global response $\bar{T}_{22} - \bar{F}_{22}$ of the composite material with the specified type of loading. (d) The variation of $\theta_{min} - \bar{F}_{22}$ of the composite material with the specified type of loading

include viscoelastic materials whose behavior ought to be described by (nonlinear) finite viscoelasticty, by adopting, for example, the viscoelastic constitutive relations suggested in Reese and Govindjee (1998). Finite strain HFGMC micromechanics for the modeling of composites in which the matrix material is represented by finite viscoelasticity was studied in Aboudi (2011).

The main qualitative difference between hyperelastic and visoelastic materials undergoing rapid, continuous, nonlocal damage, is in the symmetry breaking, which is more pronounced in the viscoelastic case. We observe that damage occurs later in the viscoelastic case. The stress response is lower, and thus the load work is lower and the dissipation is higher, and therefore the stored energy is lower and the onset of damage is delayed. On the other hand, due to the nonuniformity in material properties, loading creates stress concentration. Therefore, in the viscoelastic case, the spinodal is reached for higher loading strain and thus has more nonuniformity in the internal stress field. Therefore, at the onset of instability, there are more sources of symmetry breaking, and hence asymmetry develops faster and reaches a higher level.

Fig. 15 BK/MY composite material with a fiber volume fraction of $v_f = 0.1$. The fibers in the RUC are arranged in a hexagonal array. (a) Comparison between the variations of the global response $\bar{T}_{22} - \bar{F}_{22}$ of the viscoelastic and elastic composite materials. (b) Comparison between the variations of $\theta_{\min} - \bar{F}_{22}$ of the viscoelastic and elastic composite materials
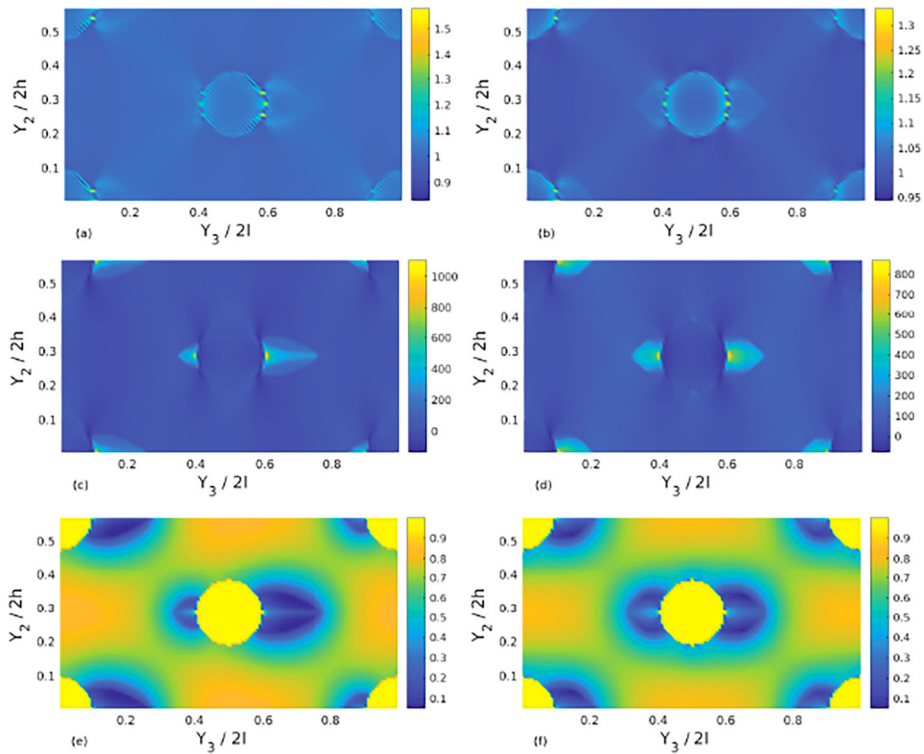
Appendix A: Internal-stresses form of the motivating rheological model

If we assume that $\frac{\partial W^{(1)}}{\partial \varepsilon} = 0$ at $t = 0$ (no internal prestress), integration by parts yields

$$\mathbf{S} = \theta \frac{\partial W^{(1)}(\mathbf{E})}{\partial \mathbf{E}} + \bar{\delta}\theta \frac{\partial W^{(1)}(\mathbf{E})}{\partial \mathbf{E}} - \frac{\bar{\delta}}{\tau_2}\theta \int_0^t e^{-(t-\tau)/\tau_2} \frac{\partial W^{(1)}(\mathbf{E}(\tau))}{\partial \mathbf{E}} d\tau. \tag{A.1}$$

It is assumed in this work that damage changes on a different scale than viscoelasticity, and θ is either nearly constant and close to unity, nearly constant and equal to zero, or changes very quickly on a time scale smaller than τ_2. In the fast time interval when θ changes, its exact temporal profile is only approximated by the solution of the intact-material continuity equation. When θ is nearly a constant, it can be inserted into the integral, whether it is close to unity or to zero. When θ changes abruptly, decreasing from unity to zero, its exact temporal profile is insignificant and thus one can also insert it into the last integral in Eq. (A.1), it would affect the result, but not qualitatively, in any case the result would be something rapidly decreasing to zero:

$$\mathbf{S} = \theta \frac{\partial W^{(1)}(\mathbf{E})}{\partial \mathbf{E}} + \bar{\delta}\theta \frac{\partial W^{(1)}(\mathbf{E})}{\partial \mathbf{E}} - \frac{\bar{\delta}}{\tau_2}\theta \int_0^{t_{\theta\sim1}} e^{-(t-\tau)/\tau_2} \frac{\partial W^{(1)}(\mathbf{E}(\tau))}{\partial \mathbf{E}} d\tau$$

$$- \frac{\bar{\delta}}{\tau_2}\theta \int_{t_{\theta\sim1}}^{t_{\theta\sim0}} e^{-(t-\tau)/\tau_2} \frac{\partial W^{(1)}(\mathbf{E}(\tau))}{\partial \mathbf{E}} d\tau - \frac{\bar{\delta}}{\tau_2}\theta \int_{t_{\theta\sim0}}^{t} e^{-(t-\tau)/\tau_2} \frac{\partial W^{(1)}(\mathbf{E}(\tau))}{\partial \mathbf{E}} d\tau \approx$$

$$\approx \theta \frac{\partial W^{(1)}(\mathbf{E})}{\partial \mathbf{E}} + \bar{\delta}\theta \frac{\partial W^{(1)}(\mathbf{E})}{\partial \mathbf{E}} - \frac{\bar{\delta}}{\tau_2} \int_0^{t_{\theta\sim1}} e^{-(t-\tau)/\tau_2}\theta \frac{\partial W^{(1)}(\mathbf{E}(\tau))}{\partial \mathbf{E}} d\tau$$

$$- \bar{\delta}\theta e^{-(t-t_{\theta\sim1/2})/\tau_2} \frac{\partial W^{(1)}(\mathbf{E}(t_{\theta\sim1/2}))}{\partial \mathbf{E}} \frac{t_{\theta\sim0} - t_{\theta\sim1}}{\tau_2} - \frac{\bar{\delta}}{\tau_2} \int_{t_{\theta\sim0}}^{t} e^{-(t-\tau)/\tau_2}\theta \frac{\partial W^{(1)}(\mathbf{E}(\tau))}{\partial \mathbf{E}} d\tau. \tag{A.2}$$

Fig. 16 BK/MY viscoelastic composite material with a fiber volume fraction of $v_f = 0.1$. The fibers in the composite are arranged in a hexagonal array. (a), (c), (e) The distributions of the deformation gradient F_{22}, the stress T_{22} (kPa), and intact-material mass fraction θ, respectively. (b), (d), (f) The corresponding distributions in the elastic case ($\tau_2 \to \infty$)

If we accept that $t_{\theta \sim 1}$ is the last instance when $\theta \sim 1$ holds, and $t_{\theta \sim 0}$ is the first instance when $\theta \sim 0$ holds, and that θ decreases form unity to zero very quickly relatively to the viscous time scale, then we observe that $t_{\theta \sim 0} - t_{\theta \sim 1} \ll \tau_2$ and therefore the contribution of the first term in the last row in Eq. (A.2) can be neglected, to yield:
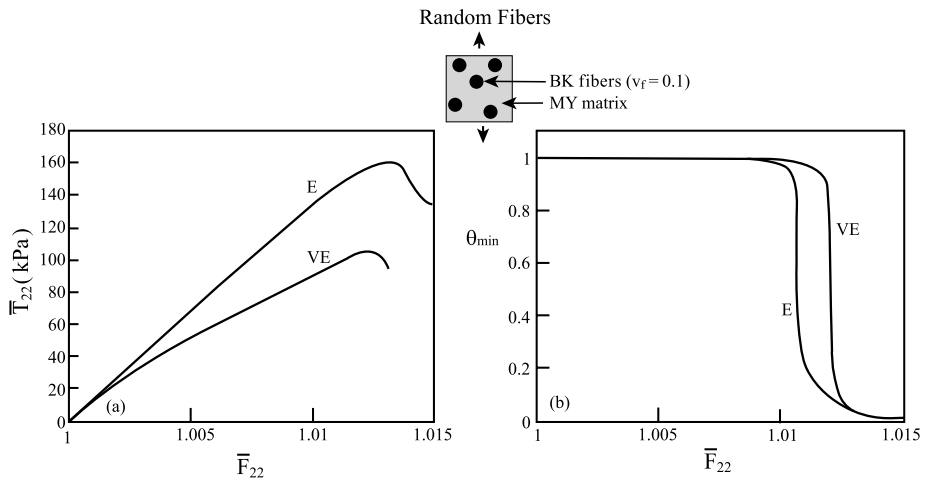
$$
\mathbf{S} = \theta \frac{\partial W^{(1)}(\mathbf{E})}{\partial \mathbf{E}} + \bar{\delta}\theta \frac{\partial W^{(1)}(\mathbf{E})}{\partial \mathbf{E}} - \frac{\bar{\delta}}{\tau_2} \int_0^{t_{\theta \sim 1}} e^{-(t-\tau)/\tau_2} \theta \frac{\partial W^{(1)}(\mathbf{E}(\tau))}{\partial \mathbf{E}} d\tau
$$
$$
- \frac{\bar{\delta}}{\tau_2} \int_{t_{\theta \sim 0}}^{t} e^{-(t-\tau)/\tau_2} \theta \frac{\partial W^{(1)}(\mathbf{E}(\tau))}{\partial \mathbf{E}} d\tau. \tag{A.3}
$$

To this we can artificially add the negligible quantity

$$
- \frac{\bar{\delta}}{\tau_2} \int_{t_{\theta \sim 1}}^{t_{\theta \sim 0}} e^{-(t-\tau)/\tau_2} \theta \frac{\partial W^{(1)}(\mathbf{E}(\tau))}{\partial \mathbf{E}} d\tau,
$$

which would yield that

$$
\mathbf{S} \approx \theta \frac{\partial W^{(1)}(\mathbf{E})}{\partial \mathbf{E}} + \bar{\delta}\theta \frac{\partial W^{(1)}(\mathbf{E})}{\partial \mathbf{E}} - \frac{\bar{\delta}}{\tau_2} \int_0^{t} e^{-(t-\tau)/\tau_2} \theta \frac{\partial W^{(1)}(\mathbf{E}(\tau))}{\partial \mathbf{E}} d\tau. \tag{A.4}
$$

Fig. 17 BK/MY composite material with a fiber volume fraction of $v_f = 0.1$. The fibers are randomly distributed in the matrix. (a) Comparison between the variations of the global response $\bar{T}_{22} - \bar{F}_{22}$ of the viscoelastic and elastic composite materials. (b) Comparison between the variations of $\theta_{\min} - \bar{F}_{22}$ of the viscoelastic and elastic composite materials

Now, if $t < t_{\theta \sim 1}$, then θ is constant, and there is no problem in inserting it into the integral. If, rather, $t > t_{\theta \sim 1}$, then the procedure as shown above becomes meaningful, and again, as demonstrated, θ can be inserted into the integral.

Finally, performing integration by parts on Eq. (A.4), we obtain

$$\mathbf{S} \approx \theta \frac{\partial W^{(1)}(\mathbf{E})}{\partial \mathbf{E}} + \bar{\delta} \int_0^t e^{-(t-\tau)/\tau_2} \frac{d}{d\tau}\left[\theta(\tau)\frac{\partial W^{(1)}(\mathbf{E}(\tau))}{\partial \mathbf{E}}\right]d\tau. \qquad (A.5)$$

Or, if we define

$$\mathbf{S}^{(1)} \triangleq \theta \frac{\partial W^{(1)}(\mathbf{E})}{\partial \mathbf{E}},$$

we remain with the simple result as follows:

$$\mathbf{S} \approx \mathbf{S}^{(1)} + \bar{\delta} \int_0^t e^{-(t-\tau)/\tau_2}\dot{\mathbf{S}}^{(1)}d\tau. \qquad (A.6)$$

As shown in Fig. 14(b), for example, the time scale of change of θ from 0.9 to 0.1 is negligible with respect to 0.25 s, which is the viscous time scale, corresponding to a change of 0.25% in the total applied strain under a strain rate of 0.01 per second. This makes the aforementioned approximation consistent and allows one working directly with macroscopic effective internal stresses, incorporating them into the standard viscoelastic theory of Simo. If the viscous time scale is faster than the time scale of damage, it is effectively elastic material, unless the loading is very rapid, in which case, special thermodynamic treatment should be given anyway, to account for possible adiabatic relations. The more straightforward case of addressing fracture in a viscoelastic material is the one considered here.
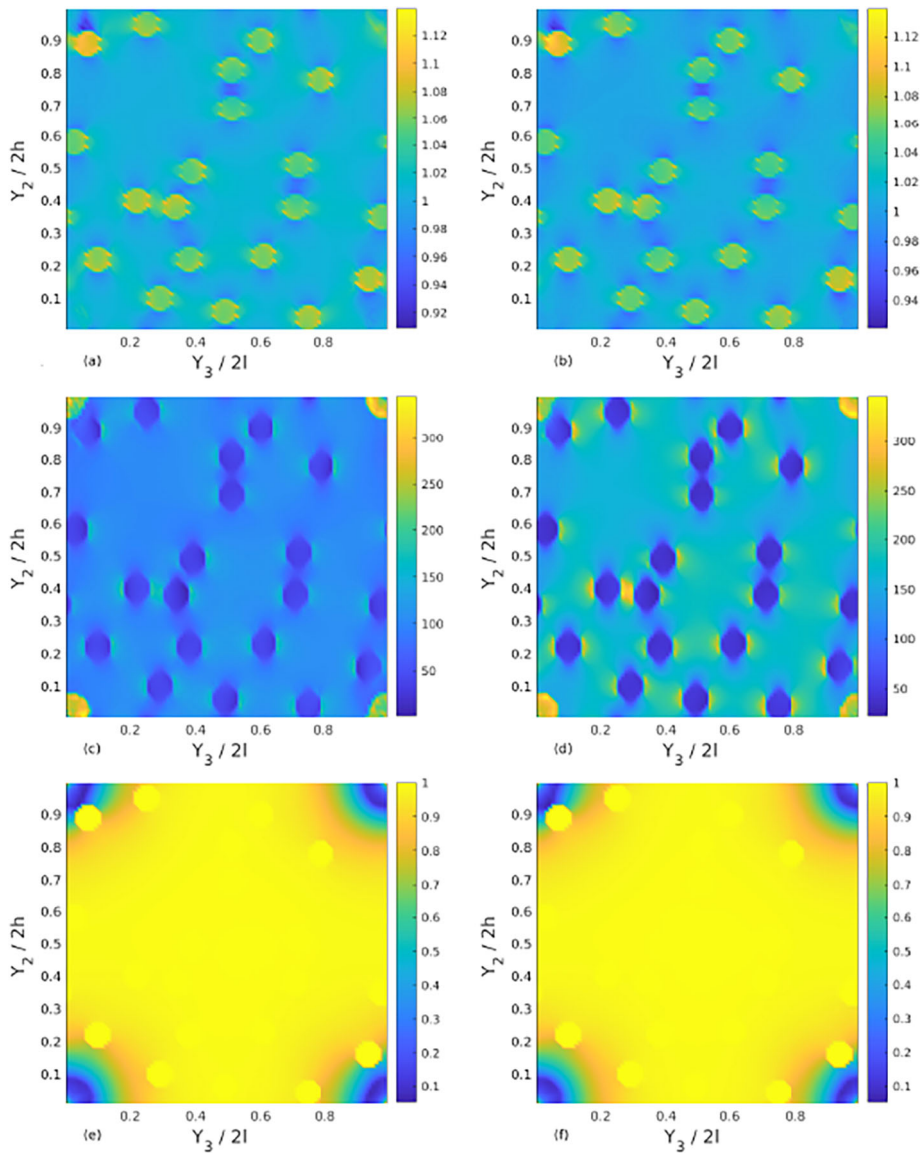
Fig. 18 BK/MY composite material with a fiber volume fraction of $v_f = 0.1$. The fibers are randomly distributed in the matrix. (a), (c), (e) The distributions of the deformation gradient F_{22}, the stress T_{22} (kPa), and the intact-material mass fraction θ, respectively. (b), (d), (f) The corresponding distributions in the elastic case ($\tau_2 \to \infty$)

Appendix B: The finite strain HFGMC micromechanics for viscoelastic composites

In the following, the details of the HFGMC micromechanical analysis of composites in which the constituents are viscoelastic materials at finite strains are presented.

The components of the increments of the deformation gradient tensor $\Delta\mathbf{F}^{(\beta\gamma)}$ in the subcell $(\beta\gamma)$ are determined from Eq. (4.2) by applying the relevant derivatives with respect to the local coordinates, as follows:

$$
\begin{aligned}
\Delta F_{11}^{(\beta\gamma)} &= \Delta\bar{F}_{11}, \quad \Delta F_{12}^{(\beta\gamma)} = \Delta\bar{F}_{12} + \Delta W_{1(10)}^{(\beta\gamma)} + 3\bar{Y}_2^{(\gamma)}\Delta W_{1(20)}^{(\beta\gamma)} \\
&\quad\quad\quad \Delta F_{13}^{(\beta\gamma)} = \Delta\bar{F}_{13} + \Delta W_{1(01)}^{(\beta\gamma)} + 3\bar{Y}_3^{(\gamma)}\Delta W_{1(02)}^{(\beta\gamma)} \\
\Delta F_{21}^{(\beta\gamma)} &= \Delta\bar{F}_{21}, \quad \Delta F_{22}^{(\beta\gamma)} = \Delta\bar{F}_{22} + \Delta W_{2(10)}^{(\beta\gamma)} + 3\bar{Y}_2^{(\gamma)}\Delta W_{2(20)}^{(\beta\gamma)} \\
&\quad\quad\quad \Delta F_{23}^{(\beta\gamma)} = \Delta\bar{F}_{23} + \Delta W_{2(01)}^{(\beta\gamma)} + 3\bar{Y}_3^{(\gamma)}\Delta W_{2(02)}^{(\beta\gamma)} \\
\Delta F_{31}^{(\beta\gamma)} &= \Delta\bar{F}_{31}, \quad \Delta F_{32}^{(\beta\gamma)} = \Delta\bar{F}_{32} + \Delta W_{3(10)}^{(\beta\gamma)} + 3\bar{Y}_2^{(\gamma)}\Delta W_{3(20)}^{(\beta\gamma)} \\
&\quad\quad\quad \Delta F_{33}^{(\beta\gamma)} = \Delta\bar{F}_{33} + \Delta W_{3(01)}^{(\beta\gamma)} + 3\bar{Y}_3^{(\gamma)}\Delta W_{3(02)}^{(\beta\gamma)}
\end{aligned}
\tag{B.1}
$$

The components of the gradient of $\Delta\theta^{(\beta\gamma)}$ in the subcell $(\beta\gamma)$ are determined from Eq. (4.3) by applying the relevant derivatives with respect to the local coordinates, as follows:

$$
\begin{aligned}
\Delta\theta_{,2}^{(\beta\gamma)} &= \Delta\theta_{2(10)}^{(\beta\gamma)} + 3\bar{Y}_2^{(\beta)}\Delta\theta_{2(20)}^{(\beta\gamma)} \\
\Delta\theta_{,3}^{(\beta\gamma)} &= \Delta\theta_{3(01)}^{(\beta\gamma)} + 3\bar{Y}_3^{(\gamma)}\Delta\theta_{3(02)}^{(\beta\gamma)}
\end{aligned}
\tag{B.2}
$$

By averaging the increments of the equilibrium equations (3.26) over the area of the subcell, the following relations are obtained:

$$
\Delta\mathbf{I}_{2(00)}^{(\beta\gamma)} + \Delta\mathbf{I}_{3(00)}^{(\beta\gamma)} = 0,
\tag{B.3}
$$

where $\Delta\mathbf{I}_{2(00)}^{(\beta\gamma)}$ and $\Delta\mathbf{I}_{3(00)}^{(\beta\gamma)}$ can be expressed in terms of the surface-averages of the traction increments evaluated along $\bar{Y}_2^{(\beta)} = \pm h_\beta/2$ and $\bar{Y}_3^{(\gamma)} = \pm l_\gamma/2$, respectively. Thus,

$$
\begin{aligned}
\Delta\mathbf{I}_{2(00)}^{(\beta\gamma)} &= \frac{1}{h_\beta}\left[\Delta\mathbf{T}_2^{+(\beta\gamma)} - \Delta\mathbf{T}_2^{-(\beta\gamma)}\right], \\
\Delta\mathbf{I}_{3(00)}^{(\beta\gamma)} &= \frac{1}{l_\gamma}\left[\Delta\mathbf{T}_3^{+(\beta\gamma)} - \Delta\mathbf{T}_3^{-(\beta\gamma)}\right],
\end{aligned}
\tag{B.4}
$$

where the surface-averages of the tractions increments are given by

$$
\begin{aligned}
\Delta\mathbf{T}_2^{\pm(\beta\gamma)} &= \frac{1}{l_\gamma}\int_{-l_\gamma/2}^{l_\gamma/2}\Delta\mathbf{\Sigma}_2^{(\beta\gamma)}\left(\bar{Y}_2^{(\beta)} = \pm\frac{h_\beta}{2}\right)d\bar{Y}_3^{(\gamma)}, \\
\Delta\mathbf{T}_3^{\pm(\beta\gamma)} &= \frac{1}{h_\beta}\int_{-h_\beta/2}^{h_\beta/2}\Delta\mathbf{\Sigma}_3^{(\beta\gamma)}\left(\bar{Y}_3^{(\gamma)} = \pm\frac{l_\gamma}{2}\right)d\bar{Y}_2^{(\beta)},
\end{aligned}
\tag{B.5}
$$

and

$$
\begin{aligned}
\Delta\mathbf{\Sigma}_2^{(\beta\gamma)} &= [\Delta T_{21}, \Delta T_{22}, \Delta T_{23}]^{(\beta\gamma)}, \\
\Delta\mathbf{\Sigma}_3^{(\beta\gamma)} &= [\Delta T_{31}, \Delta T_{32}, \Delta T_{33}]^{(\beta\gamma)}.
\end{aligned}
\tag{B.6}
$$

The two vectors $\Delta \boldsymbol{\Sigma}_2^{(\beta\gamma)}$ and $\Delta \boldsymbol{\Sigma}_3^{(\beta\gamma)}$ include the tractions increments acting on the surfaces whose normals are in the $\bar{Y}_2^{(\beta)}$ and $\bar{Y}_3^{(\gamma)}$ directions, respectively.

Substitution of Eq. (B.4) in (B.3) yields

$$\frac{1}{h_\beta}\left[\Delta \mathbf{T}_2^{+(\beta\gamma)} - \Delta \mathbf{T}_2^{-(\beta\gamma)}\right] + \frac{1}{l_\gamma}\left[\Delta \mathbf{T}_3^{+(\beta\gamma)} - \Delta \mathbf{T}_3^{-(\beta\gamma)}\right] = 0 \tag{B.7}$$

This equation expresses the increments of the equilibrium equations imposed in the average sense within subcell $(\beta\gamma)$.

By employing the constitutive relations (3.25), the following expressions for the surface-averages of the tractions increments are obtained from Eqs. (B.1) and (B.5):

$$\Delta T_{2i}^{\pm(\beta\gamma)} = Z_{k2}^{(\beta\gamma)}\left(\Delta W_{1(10)} \pm \frac{3h_\beta}{2}\Delta W_{1(20)}\right)^{(\beta\gamma)} + Z_{k3}^{(\beta\gamma)}\Delta W_{1(01)}^{(\beta\gamma)}$$

$$+ Z_{k5}^{(\beta\gamma)}\left(\Delta W_{2(10)} \pm \frac{3h_\beta}{2}\Delta W_{2(20)}\right)^{(\beta\gamma)} + Z_{k6}^{(\beta\gamma)}\Delta W_{2(01)}^{(\beta\gamma)}$$

$$+ Z_{k8}^{(\beta\gamma)}\left(\Delta W_{3(10)} \pm \frac{3h_\beta}{2}\Delta W_{3(20)}\right)^{(\beta\gamma)} + Z_{k9}^{(\beta\gamma)}\Delta W_{3(01)}^{(\beta\gamma)} \tag{B.8}$$

$$+ \sum_{p=1}^{9} Z_{kp}^{(\beta\gamma)}\Delta\bar{\Omega}_p + H_{2i}^{(\beta\gamma)}\left(\Delta\theta_{(00)} \pm \frac{h_\beta}{2}\Delta\theta_{(10)} + \frac{3h_\beta}{2}\Delta\theta_{(20)}\right)^{(\beta\gamma)} - \Delta V_{2i}^{(\beta\gamma)},$$

where $i = 1 \rightarrow k = 4$, $i = 2 \rightarrow k = 5$, $i = 3 \rightarrow k = 6$.

$$\Delta T_{3i}^{\pm(\beta\gamma)} = Z_{k2}^{(\beta\gamma)}\Delta W_{1(10)}^{(\beta\gamma)} + Z_{k3}^{(\beta\gamma)}\left(\Delta W_{1(01)} \pm \frac{3l_\gamma}{2}\Delta W_{1(02)}\right)^{(\beta\gamma)}$$

$$+ Z_{k5}^{(\beta\gamma)}\Delta W_{2(10)}^{(\beta\gamma)} + Z_{k6}^{(\beta\gamma)}\left(\Delta W_{2(01)} \pm \frac{3l_\gamma}{2}\Delta W_{2(02)}\right)^{(\beta\gamma)}$$

$$+ Z_{k8}^{(\beta\gamma)}\Delta W_{3(10)}^{(\beta\gamma)} + Z_{k9}^{(\beta\gamma)}\left(\Delta W_{3(01)} \pm \frac{3l_\gamma}{2}\Delta W_{3(02)}\right)^{(\beta\gamma)} \tag{B.9}$$

$$+ \sum_{p=1}^{9} Z_{kp}^{(\beta\gamma)}\Delta\bar{\Omega}_p + H_{3i}^{(\beta\gamma)}\left(\Delta\theta_{(00)} \pm \frac{l_\gamma}{2}\Delta\theta_{(01)} + \frac{3l_\gamma}{2}\Delta\theta_{(02)}\right)^{(\beta\gamma)} - \Delta V_{3i}^{(\beta\gamma)},$$

where $i = 1 \rightarrow k = 7$, $i = 2 \rightarrow k = 8$, $i = 3 \rightarrow k = 9$. In these equations, $\Delta\bar{\boldsymbol{\Omega}}$ represents the applied far-field:

$$\Delta\bar{\boldsymbol{\Omega}} = \left[\Delta\bar{F}_{11}, \Delta\bar{F}_{12}, \Delta\bar{F}_{13}, \Delta\bar{F}_{21}, \Delta\bar{F}_{22}, \Delta\bar{F}_{23}, \Delta\bar{F}_{31}, \Delta\bar{F}_{32}, \Delta\bar{F}_{33}\right]. \tag{B.10}$$

Substitution of Eqs. (B.8)–(B.9) in Eq. (B.7) provides the three relations:

$$\left[Z_{22}\Delta W_{1(20)} + Z_{25}\Delta W_{2(20)} + Z_{28}\Delta W_{3(20)} + Z_{33}\Delta W_{1(02)} + Z_{36}\Delta W_{2(02)} + Z_{39}\Delta W_{3(02)}\right.$$

$$\left. + H_{21}\Delta\theta_{(10)} + H_{31}\Delta\theta_{(01)} - \Delta V_{21} - \Delta V_{31}\right]^{(\beta\gamma)} = 0 \tag{B.11}$$

$$\left[Z_{52}\Delta W_{1(20)} + Z_{55}\Delta W_{2(20)} + Z_{58}\Delta W_{3(20)} + Z_{63}\Delta W_{1(02)} + Z_{66}\Delta W_{2(02)} + Z_{69}\Delta W_{3(02)} \right.$$

$$\left. + H_{22}\Delta\theta_{(10)} + H_{32}\Delta\theta_{(01)} - \Delta V_{22} - \Delta V_{32} \right]^{(\beta\gamma)} = 0 \tag{B.12}$$

$$\left[Z_{82}\Delta W_{1(20)} + Z_{85}\Delta W_{2(20)} + Z_{88}\Delta W_{3(20)} + Z_{93}\Delta W_{1(02)} + Z_{96}\Delta W_{2(02)} + Z_{99}\Delta W_{3(02)} \right.$$

$$\left. + H_{23}\Delta\theta_{(10)} + H_{33}\Delta\theta_{(01)} - \Delta V_{23} - \Delta V_{33} \right]^{(\beta\gamma)} = 0 \tag{B.13}$$

These three relations express the increments of the average equilibrium equations (3.26) in the subcell, which are given in terms of the increments of the unknown micromechanical variables $\Delta\mathbf{W}_{(mn)}^{(\beta\gamma)}$.

As to the mass flux $\mathbf{s}$, let us define the surface averages of the increments $\Delta\mathbf{s}^{\pm(\beta\gamma)}$ in the subcells as follows:

$$\Delta s_2^{\pm(\beta\gamma)} = \frac{1}{l_\gamma} \int_{-l_\gamma/2}^{l_\gamma/2} \Delta s_2^{(\beta\gamma)} \left(\bar{Y}_2^{(\beta)} = \pm\frac{h_\beta}{2} \right) d\bar{Y}_3^{(\gamma)}$$

$$\Delta s_3^{\pm(\beta\gamma)} = \frac{1}{h_\beta} \int_{-h_\beta/2}^{h_\beta/2} \Delta s_3^{(\beta\gamma)} \left(\bar{Y}_3^{(\gamma)} = \pm\frac{l_\gamma}{2} \right) d\bar{Y}_2^{(\beta)} \tag{B.14}$$

and

$$\Delta J_{2(00)}^{(\beta\gamma)} = \frac{1}{h_\beta} \left[\Delta s_2^{+(\beta\gamma)} - \Delta s_2^{-(\beta\gamma)} \right]$$

$$\Delta J_{3(00)}^{(\beta\gamma)} = \frac{1}{l_\gamma} \left[\Delta s_3^{+(\beta\gamma)} - \Delta s_3^{-(\beta\gamma)} \right] \tag{B.15}$$

With these definitions, the average of the incremental mass balance (3.2) yields:

$$\Delta J_{2(00)}^{(\beta\gamma)} + \Delta J_{3(000)}^{(\beta\gamma)} - \Delta\chi^{(\beta\gamma)} = 0, \tag{B.16}$$

where

$$\Delta\chi^{(\beta\gamma)} = \frac{1}{h_\beta l_\gamma} \int_{-h_\beta}^{h_\beta} \int_{-l_\gamma}^{l_\gamma} \left[E_1\Delta\theta + E_2\Delta W^{(1)} \right]^{(\beta\gamma)} d\bar{Y}_2^{(\beta)} d\bar{Y}_3^{(\gamma)}$$

$$= \left\{ E_1\Delta\theta_{(00)} + E_2 \left[H_{12}\Delta W_{1(10)} + H_{13}\Delta W_{1(01)} \right. \right. \tag{B.17}$$

$$\left. \left. + H_{22}\Delta W_{2(10)} + H_{23}\Delta W_{2(01)} + H_{32}\Delta W_{3(10)} + H_{33}\Delta W_{3(01)} \right] \right\}^{(\beta\gamma)}.$$

Thus,

$$\frac{1}{h_\beta}\left(\Delta s_2^{+(\beta\gamma)} - \Delta s_2^{-(\beta\gamma)} \right) + \frac{1}{l_\gamma}\left(\Delta s_3^{+(\beta\gamma)} - \Delta s_3^{-(\beta\gamma)} \right) - \Delta\chi^{(\beta\gamma)} = 0 \tag{B.18}$$

and

$$E_1^{(\beta\gamma)} = \frac{1}{1/\zeta^{(\beta\gamma)} + \epsilon}, \quad E_2^{(\beta\gamma)} = \left[\frac{\theta}{(1 + \epsilon\zeta)^2} \frac{m}{\phi} \left(\frac{W^{(1)}}{\phi} \right)^{m-1} \zeta \right]^{(\beta\gamma)}, \qquad \text{(B.19)}$$

which are already known from the previous step.

Similarly to the increments of the surface-averaged tractions and mass fluxes, which were defined in Eq. (B.5) and (B.14), the surface-averaged displacement increments can be defined by

$$\Delta \mathbf{U}_2^{\pm(\beta\gamma)} = \frac{1}{l_\gamma} \int_{-l_\gamma/2}^{l_\gamma/2} \Delta \mathbf{W}^{(\beta\gamma)} \left(\bar{Y}_2^{(\beta)} = \pm \frac{h_\beta}{2} \right) d\bar{Y}_3^{(\gamma)},$$

$$\Delta \mathbf{U}_3^{\pm(\beta\gamma)} = \frac{1}{h_\beta} \int_{-h_\beta/2}^{h_\beta/2} \Delta \mathbf{W}^{(\beta\gamma)} \left(\bar{Y}_3^{(\gamma)} = \pm \frac{l_\gamma}{2} \right) d\bar{Y}_2^{(\beta)}. \qquad \text{(B.20)}$$

In the following, these increments of the surface-averaged quantities $\Delta \mathbf{U}_i^{\pm(\beta\gamma)}$, $i = 2, 3$, will be related to the increments of the microvariables $\mathbf{W}_{(mn)}^{(\beta\gamma)}$, $(mn) = 0, 1, 2$; in the expansions (4.2). To this end, by substituting (4.2) in (B.20), the following relations are obtained:

$$\Delta \mathbf{U}_2^{\pm(\beta\gamma)} = \Delta \mathbf{W}_{(00)}^{(\beta\gamma)} \pm \frac{h_\beta}{2} \Delta \mathbf{W}_{(10)}^{(\beta\gamma)} + \frac{h_\beta^2}{4} \Delta \mathbf{W}_{(20)}^{(\beta\gamma)},$$

$$\Delta \mathbf{U}_3^{\pm(\beta\gamma)} = \Delta \mathbf{W}_{(00)}^{(\beta\gamma)} \pm \frac{l_\gamma}{2} \Delta \mathbf{W}_{(01)}^{(\beta\gamma)} + \frac{l_\gamma^2}{4} \Delta \mathbf{W}_{(02)}^{(\beta\gamma)}. \qquad \text{(B.21)}$$

Manipulations of Eq. (B.21) by subtractions and additions yield

$$\Delta \mathbf{W}_{(10)}^{(\beta\gamma)} = \frac{1}{h_\beta} \left[\Delta \mathbf{U}_2^+ - \Delta \mathbf{U}_2^- \right]^{(\beta\gamma)},$$

$$\Delta \mathbf{W}_{(01)}^{(\beta\gamma)} = \frac{1}{l_\gamma} \left[\Delta \mathbf{U}_3^+ - \Delta \mathbf{U}_3^- \right]^{(\beta\gamma)}, \qquad \text{(B.22)}$$

and

$$\Delta \mathbf{W}_{(20)}^{(\beta\gamma)} = \frac{2}{h_\beta^2} \left[\Delta \mathbf{U}_2^+ + \Delta \mathbf{U}_2^- \right]^{(\beta\gamma)} - \frac{4}{h_\beta^2} \Delta \mathbf{W}_{(00)}^{(\beta\gamma)},$$

$$\Delta \mathbf{W}_{(02)}^{(\beta\gamma)} = \frac{2}{l_\gamma^2} \left[\Delta \mathbf{U}_3^+ + \Delta \mathbf{U}_3^- \right]^{(\beta\gamma)} - \frac{4}{l_\gamma^2} \Delta \mathbf{W}_{(00)}^{(\beta\gamma)}. \qquad \text{(B.23)}$$

Similarly, we define:

$$\Delta \theta_2^{\pm(\beta\gamma)} = \frac{1}{l_\gamma} \int_{-l_\gamma/2}^{l_\gamma/2} \Delta \theta^{(\beta\gamma)} \left(\bar{Y}_2^{(\beta)} = \pm \frac{h_\beta}{2} \right) d\bar{Y}_3^{(\gamma)},$$

$$\Delta \theta_3^{\pm(\beta\gamma)} = \frac{1}{h_\beta} \int_{-h_\beta/2}^{h_\beta/2} \Delta \theta^{(\beta\gamma)} \left(\bar{Y}_3^{(\gamma)} = \pm \frac{l_\gamma}{2} \right) d\bar{Y}_2^{(\beta)}. \qquad \text{(B.24)}$$

By employing the expansion of $\Delta\theta$ in Eq. (4.3), we obtain:

$$\Delta \theta_2^{\pm(\beta\gamma)} = \Delta \theta_{(00)}^{(\beta\gamma)} \pm \frac{h_\beta}{2} \Delta \theta_{(10)}^{(\beta\gamma)} + \frac{h_\beta^2}{4} \Delta \theta_{(20)}^{(\beta\gamma)},$$

$$\Delta\theta_3^{\pm(\beta\gamma)} = \Delta\theta_{(00)}^{(\beta\gamma)} \pm \frac{l_\gamma}{2}\Delta\theta_{(01)}^{(\beta\gamma)} + \frac{l_\gamma^2}{4}\Delta\theta_{(02)}^{(\beta\gamma)}. \tag{B.25}$$

Manipulations of Eq. (B.25) by subtractions and additions yield

$$\Delta\theta_{(10)}^{(\beta\gamma)} = \frac{1}{h_\beta}\left[\Delta\theta_2^+ - \Delta\theta_2^-\right]^{(\beta\gamma)},$$

$$\Delta\theta_{(01)}^{(\beta\gamma)} = \frac{1}{l_\gamma}\left[\Delta\theta_3^+ - \Delta\theta_3^-\right]^{(\beta\gamma)}, \tag{B.26}$$

and

$$\Delta\theta_{(20)}^{(\beta\gamma)} = \frac{2}{h_\beta^2}\left[\Delta\theta_2^+ + \Delta\theta_2^-\right]^{(\beta\gamma)} - \frac{4}{h_\beta^2}\Delta\theta_{(00)}^{(\beta\gamma)},$$

$$\Delta\theta_{(02)}^{(\beta\gamma)} = \frac{2}{l_\gamma^2}\left[\Delta\theta_3^+ + \Delta\theta_3^-\right]^{(\beta\gamma)} - \frac{4}{l_\gamma^2}\Delta\theta_{(00)}^{(\beta\gamma)}. \tag{B.27}$$

It is now possible to express $\Delta\mathbf{W}_{(00)}^{(\beta\gamma)}$ in terms of the surface-averaged displacement increments $\Delta\mathbf{U}_i^{\pm(\beta\gamma)}$; $i = 2, 3$. This is achieved by substituting Eqs. (B.22)–(B.23) in (B.11)–(B.13). As a result, a system of three linear algebraic equations in the three unknowns $\Delta\mathbf{W}_{(00)}^{(\beta\gamma)}$ is obtained. The solution of this system of equations expresses these microvariables in terms of $\Delta\mathbf{U}_i^{\pm(\beta\gamma)}$ and $\Delta\theta_i^{\pm(\beta\gamma)}$; $i = 2, 3$. As to $\Delta\theta_{(00)}^{(\beta\gamma)}$, it can be determined by substituting (B.26) and (B.27) in the incremental mass balance (B.16). Hence, these solutions, together with Eqs. (B.22)–(B.23) and (B.26)–(B.27), can be represented as follows:

$$\begin{Bmatrix} \Delta\mathbf{W}_{(00)} \\ \Delta\mathbf{W}_{(10)} \\ \Delta\mathbf{W}_{(01)} \\ \Delta\mathbf{W}_{(20)} \\ \Delta\mathbf{W}_{(02)} \\ \Delta\theta_{(00)} \\ \Delta\theta_{(10)} \\ \Delta\theta_{(01)} \\ \Delta\theta_{(20)} \\ \Delta\theta_{(02)} \end{Bmatrix}^{(\beta\gamma)} = \mathbf{M}^{(\beta\gamma)} \begin{Bmatrix} \Delta\mathbf{U}_2^+ - \Delta\mathbf{U}_2^- \\ \Delta\mathbf{U}_3^+ - \Delta\mathbf{U}_3^- \\ \Delta\theta_2^+ - \Delta\theta_2^- \\ \Delta\theta_3^+ - \Delta\theta_3^- \end{Bmatrix}^{(\beta\gamma)}, \tag{B.28}$$

where $\mathbf{M}_i^{(\beta\gamma)}$ are matrices whose elements are lengthy and therefore are not shown here.

Consequently, with expressions (B.28), the following relations can be established from Eqs. (B.8)–(B.9):

$$\begin{Bmatrix} \Delta\mathbf{T}_2^\pm \\ \Delta\mathbf{T}_3^\pm \\ \Delta s_2^\pm \\ \Delta s_3^\pm \end{Bmatrix}^{(\beta\gamma)} = \mathbf{K}^{(\beta\gamma)} \begin{Bmatrix} \Delta\mathbf{U}_2^\pm \\ \Delta\mathbf{U}_3^\pm \\ \Delta\theta_2^\pm \\ \Delta\theta_3^\pm \end{Bmatrix}^{(\beta\gamma)} + \begin{Bmatrix} \Delta\boldsymbol{\Phi}_2^\pm \\ \Delta\boldsymbol{\Phi}_3^\pm \\ 0 \\ 0 \end{Bmatrix}^{(\beta\gamma)} - \begin{Bmatrix} \Delta\mathbf{V}_2^\pm \\ \Delta\mathbf{V}_3^\pm \\ 0 \\ 0 \end{Bmatrix}^{(\beta\gamma)}, \tag{B.29}$$

where $\mathbf{K}^{(\beta\gamma)}$ is a square 16×16 matrix consistent of the instantaneous properties $\mathbf{Z}^{(\beta\gamma)}$ of the material filling subcell $(\beta\gamma)$, and its geometrical dimensions. In these equations, the

vectors $\Delta\boldsymbol{\Phi}_i^{\pm(\beta\gamma)}$, $i = 2, 3$; are the far-field contributions. They are defined by

$$\Delta\boldsymbol{\Phi}_2^{\pm(\beta\gamma)} = \left[\sum_{p=1}^{9} Z_{4p}^{(\beta\gamma)}\Delta\bar{\Omega}_p, \quad \sum_{p=1}^{9} Z_{5p}^{(\beta\gamma)}\Delta\bar{\Omega}_p, \quad \sum_{p=1}^{9} Z_{6p}^{(\beta\gamma)}\Delta\bar{\Omega}_p \right]$$

$$\Delta\boldsymbol{\Phi}_3^{\pm(\beta\gamma)} = \left[\sum_{p=1}^{9} Z_{7p}^{(\beta\gamma)}\Delta\bar{\Omega}_p, \quad \sum_{p=1}^{9} Z_{8p}^{(\beta\gamma)}\Delta\bar{\Omega}_p, \quad \sum_{p=1}^{9} Z_{9p}^{(\beta\gamma)}\Delta\bar{\Omega}_p \right] \tag{B.30}$$

In addition,

$$\Delta\mathbf{V}_2^{\pm(\beta\gamma)} = [\Delta V_{21}, \quad \Delta V_{22}, \quad \Delta V_{23}]^{(\beta\gamma)},$$

$$\Delta\mathbf{V}_3^{\pm(\beta\gamma)} = [\Delta V_{31}, \quad \Delta V_{32}, \quad \Delta V_{33}]^{(\beta\gamma)}. \tag{B.31}$$

The continuity conditions of surface-averaged displacement increments and surface-averaged traction increments between neighboring subcells require that

$$[\Delta\mathbf{U}_2 \quad \Delta\mathbf{T}_2]^{+(\beta\gamma)} = [\Delta\mathbf{U}_2 \quad \Delta\mathbf{T}_2]^{-(\beta+1\,\gamma)}, \quad \beta = 1, \dots, N_\beta - 1, \ \gamma = 1, \dots, N_\gamma,$$

$$[\Delta\mathbf{U}_3 \quad \Delta\mathbf{T}_3]^{+(\beta\gamma)} = [\Delta\mathbf{U}_3 \quad \Delta\mathbf{T}_3]^{-(\beta\,\gamma+1)}, \quad \beta = 1, \dots, N_\beta, \ \gamma = 1, \dots, N_\gamma - 1 \tag{B.32}$$

In addition, similar relations hold for the mass ratios and fluxes:

$$[\Delta\theta_2 \quad \Delta s_2]^{+(\beta\gamma)} = [\Delta\theta_2 \quad \Delta s_2]^{-(\beta+1\,\gamma)}, \quad \beta = 1, \dots, N_\beta - 1, \ \gamma = 1, \dots, N_\gamma,$$

$$[\Delta\theta_3 \quad \Delta s_3]^{+(\beta\gamma)} = [\Delta\theta_3 \quad \Delta s_3]^{-(\beta\,\gamma+1)}, \quad \beta = 1, \dots, N_\beta, \ \gamma = 1, \dots, N_\gamma - 1. \tag{B.33}$$

Next, the periodicity conditions that require equality between the surface-averaged displacement increments (as well as the surface-averaged traction increments) at the opposite sides of the RUC are

$$[\Delta\mathbf{U}_2 \quad \Delta\mathbf{T}_2]^{-(1\gamma)} = [\Delta\mathbf{U}_2 \quad \Delta\mathbf{T}_2]^{+(N_\beta\,\gamma)}, \quad \gamma = 1, \dots, N_\gamma,$$

$$[\Delta\mathbf{U}_3 \quad \Delta\mathbf{T}_3]^{-(\beta 1)} = [\Delta\mathbf{U}_3 \quad \Delta\mathbf{T}_3]^{+(\beta\,N_\gamma)}, \quad \beta = 1, \dots, N_\beta. \tag{B.34}$$

Similarly,

$$[\Delta\theta_2 \quad \Delta s_2]^{-(1\gamma)} = [\Delta\theta_2 \quad \Delta s_2]^{+(N_\beta\,\gamma)}, \quad \gamma = 1, \dots, N_\gamma$$

$$[\Delta\theta_3 \quad \Delta s_3]^{-(\beta 1)} = [\Delta\theta_3 \quad \Delta s_3]^{+(\beta\,N_\gamma)}, \quad \beta = 1, \dots, N_\beta \tag{B.35}$$

Equations (B.32)-(B.35) form a system of $16N_\beta N_\gamma$ algebraic equations of the same number as the surface-averaged displacement increments $\Delta\mathbf{U}_2^{\pm(\beta\gamma)}$, $\Delta\mathbf{U}_3^{\pm(\beta\gamma)}$ and the surface-averaged increments $\Delta\theta_2^{\pm(\beta\gamma)}$, $\Delta\theta_3^{\pm(\beta\gamma)}$ in all the subcells of the RUC (i.e., the composite). This system can be represented as:

$$\begin{bmatrix} \mathbf{A}_{11} & \mathbf{A}_{12} \\ \mathbf{A}_{21} & \mathbf{A}_{22} \end{bmatrix} \begin{Bmatrix} \Delta\mathbf{U}^\pm \\ \Delta\boldsymbol{\theta}^\pm \end{Bmatrix} = \begin{bmatrix} \Delta\boldsymbol{\Phi}^\pm(\Delta\bar{\mathbf{F}}) - \Delta\mathbf{V}^\pm \\ \mathbf{0} \end{bmatrix}, \tag{B.36}$$

where $\Delta\boldsymbol{\Phi}^\pm$ and $\Delta\mathbf{V}^\pm$ denote the applied mechanical far-field and viscoelastic terms increments, respectively.

Author contributions J.A. developed the main part of the HFGMC solver, programmed the predictor-corrector scheme, obtained the numerical results, wrote part of the draft and produced part of the figures; K.Y. proposed the damage model and the way to incorporate viscosity; N.P. developed the predictor-corrector scheme, finalized the motivation for the damage model, validated the motivation for the form of incorporation of viscosity, obtained the analytical results, wrote part of the draft, produced part of the figures and made the final editing.

Data Availability No datasets were generated or analysed during the current study.

Declarations

Competing interests The authors declare no competing interests.

References

https://www.biorender.com/

Aboudi, J.: Micromechanical modeling of viscoelastic behavior of polymer matrix composites undergoing large deformations. In: Guedes, R.M. (ed.) Creep and Fatigue of Polymer Matrix Composites, pp. 302–324. Woodhead Pub. Ltd., Oxford (2011)

Aboudi, J., Volokh, K.Y.: Modeling deformation and failure of viscoelastic composites at finite strains. Mech. Soft Mater. **2**, 12 (2020)

Aboudi, J., Arnold, S.M., Bednarcyk, B.A.: Micromechanics of Composite Materials: A Generalized Multiscale Analysis Approach. Elsevier, Oxford (2013)

Abu-Qbeitah, S., Jabareen, M., Volokh, K.Y.: Dynamic versus quasi-static analysis of crack propagation in soft materials. J. Appl. Mech. **89**, 121008 (2022)

Abu-Qbeitah, S., Jabareen, M., Volokh, K.Y.: Quasi-static crack propagation in soft materials using the material-sink theory. Int. J. Mech. Sci. **248**, 108160 (2023a)

Abu-Qbeitah, S., Jabareen, M., Volokh, K.Y.: Modeling cracks in viscoelastic materials at finite strains. Int. J. Numer. Methods Eng. (2023b). https://doi.org/10.1002/nme.7398

Arash, B., Exner, W., Rolfes, R.: A finite deformation phase-field fracture model for the thermo-viscoelastic analysis of polymer nanocomposites. Comput. Methods Appl. Mech. Eng. **381**, 113821 (2021)

Blatz, P.J., Ko, W.L.: Application of finite elastic theory to the deformation of rubbery materials. Trans. Soc. Rheol. **6**, 223–251 (1962)

Breiman, U., Meshi, I., Aboudi, J., Haj-Ali, R.: Finite strain parametric HFGMC micromechanics of soft tissues. Biomech. Model. Mechanobiol. **19**, 2443–2453 (2020)

Breiman, U., Meshi, I., Aboudi, J., Haj-Ali, R.: Finite strain PHFGMC micromechanics with damage and failure. Acta Mech. **233**, 1615–2651 (2022)

Britannica, The Editors of Encyclopaedia: "Artery". Encyclopedia Britannica 30 Nov. (2023). https://www.britannica.com/science/artery

Bui, T.Q., Hu, X.: A review of phase-field models, fundamentals and their applications to composite laminates. Eng. Fract. Mech. **248**, 107705 (2021)

Dammaß, F., Kalina, K.A., Ambatl, M., Kästner, M.: Phase-field modelling and analysis of rate-dependent fracture phenomena at finite deformation. Comput. Mech. **72**, 859–883 (2023)

Dormieux, L., Kondo, D.: Micromechanics of Fracture and Damage. Wiley, New York (2016)

Fantoni, F., Bacigalupo, A., Paggi, M., et al.: A phase field approach for damage propagation in periodic microstructured materials. Int. J. Fract. **223**, 53–76 (2020)

Faye, A., Lev, Y., Volokh, K.Y.: The effect of local inertia around the crack tip in dynamic fracture of soft materials. Mech. Soft Mater. **1**(4) (2019)

Gopalsamy, R., Chevaugeon, N., Chupin, O., Hammoum, F.: Variational approach to viscoelastic fracture: comparison of a phase-field and of a lip-field approach. Int. J. Fract. **244**, 163–185 (2023)

Hai, L., Wriggers, P., Huang, Y., Zhang, H., Xu, S.: Dynamic fracture investigation of concrete by a rate-dependent explicit phase field model integrating viscoelasticity and micro-viscosity. Comput. Methods Appl. Mech. Eng. **418**, 116540 (2024)

Holzapfel, G.A.: Nonlinear Solid Mechanics. Wiley, New York (2000)

Hu, P., Dong, C., Zhen, H., Xu, C., Zhang, C.: Higher-order phase field fracture simulation in nearly incompressible viscoelasticity. Eng. Fract. Mech. **293**(1), 109655 (2023)

Jafarzadeh, H., Shchyglo, O., Steinbach, I.: Multi-phase-field approach to fracture demonstrating the role of solid-solid interface energy on crack propagation. Int. J. Fract. **245**, 75–87 (2024)

Kachanov, L.: Introduction to Continuum Damage Mechanics (Vol. 10). Springer, Berlin (1986)

Malvern, L.E.: Intoduction to the Mechanics of Continuous Medium. Prentice Hall, Englewood Cliff (1969)

Meshi, I., Breiman, U., Haj-Ali, R.: The parametric high-fidelity-generalized-method-of-cells with phase-field damage micromechanical model for heterogeneous composites. Compos. Struct. **320**, 117199 (2023)

Miehe, C., Hofacker, M., Welschinger, F.: A phase field model for rate-independent crack propagation: robust algorithmic implementation based on operator splits. Comput. Methods Appl. Mech. Eng. **199**(45–48), 2765–2778 (2010)

Murakami, S.: Continuum Damage Mechanics: A Continuum Mechanics Approach to the Analysis of Damage and Fracture, vol. 185. Springer, Berlin (2012)

Murthy, P.L.N., Bednarcyk, B.A., Mital, S.K.: A Compilation of Matlab Scripts and Functions for MAC/GMC Analyses. NASA/TM-2017-219500, Glenn Research Center, Cleveland, Ohio 44135

Partmann, K., Wieners, C., Weinberg, K.: Continuum-kinematics-based peridynamics and phase-field approximation of non-local dynamic fracture. Int. J. Fract. **244**, 187–200 (2023)

Perchikov, N., Aboudi, J., Volokh, K.Y.: Finite strain HFGMC analysis of damage evolution in nonlinear periodic composite materials. Arch. Appl. Mech. **93**, 4361–4386 (2023)

Polyanin, A.D., Zaitsev, V.F.: Handbook of Exact Solutions for Ordinary Differential Equations, 2nd edn. Chapman & Hall, Boca Raton (2003)

Quinteros, M., Garcia-Maciaz, E., Martinez-Paneda, E.: Micromechanics-based phase field fracture modelling of CNT composites. Composites, Part B, Eng. **236**, 109788 (2022)

Rao, S., Budzik, M.K., Dias, M.A.: On microscopic analysis of fracture in unidirectional composite material using phase field modelling. Compos. Sci. Technol. **220**, 109242 (2022)

Reese, S., Govindjee, S.: A theory of finite viscoelasticity and numerical aspects. Int. J. Solids Struct. **35**, 3455–3482 (1998)

Ritchie, R.O., Liu, D.: Introduction to Fracture Mechanics. Elsevier, Amsterdam (2021)

Sangaletti, S., Garcia, L.G.: Fracture tailoring in 3D printed continuous fibre composite materials using the phase field approach for fracture. Compos. Struct. **300**, 116127 (2022)

Simo, J.C.: On a fully three-dimensional finite-strain viscoelastic damage model: reformulation and computational aspects. Comput. Methods Appl. Mech. Eng. **60**, 153–173 (1987)

Simo, J.C., Hughes, T.J.R.: Computational Inelasticty. Springer, New York (1998)

Volokh, K.Y.: Mechanics of Soft Materials. Springer, Berlin (2016)

Volokh, K.Y.: Fracture as a material sink. J. Mater. Sci. Mater. Theory **1**, 1–9 (2017)

Volokh, K.Y.: New approaches to modeling failure and fracture of rubberlike materials. In: Fatigue Crack Growth in Rubber Materials. Advances in Polymer Science, vol. 286, pp. 131–152. Springer, Berlin (2020)